

Spatiotemporal dynamics of nanosecond pulsed discharge in the form of a fast ionization wave: self-consistent two-dimensional modeling and comparison with experiments under negative and positive polarity.

Konstantinos Kourtzanidis

Chemical Process & Energy Resources Institute (CPERI), Centre for Research & Technology Hellas (CERTH), 6th km Charilaou-Thermi, Thermi, 57001 Thessaloniki, Greece

Svetlana M. Starikovskaia

Laboratory of Plasma Physics (CNRS, Ecole Polytechnique, Univ. Paris-Sud, Observatoire de Paris, Sorbonne Université, l'Institut Polytechnique de Paris), Ecole Polytechnique, route de Saclay, 91128 Palaiseau, France

E-mail: kourtzanidis@certh.gr

Abstract.

Nanosecond discharges are characterized by a shift in energy branching toward the excitation of electronic levels and dissociation, making them particularly attractive for plasma chemistry. Understanding the spatio-temporal structure of these discharges is especially important. This paper presents a detailed 2D-axisymmetric numerical analysis of a nanosecond discharge propagating in a long tube and in pure nitrogen. The modeling is conducted using a self-consistent plasma fluid solver under the local mean energy approximation (LMEA), including photoionization. The discharge develops at moderate pressures, 1–10 Torr, in the form of a fast ionization wave (FIW). Simulations are performed for both negative and positive polarities of the voltage pulse applied to the high-voltage electrode. The computational results are validated against available experimental data, including FIW velocity within the studied pressure range, electron density, longitudinal electric field, and the radial distribution of $N_2(C^3\Pi_u)$ emission on a nanosecond timescale.

1. Introduction

Nanosecond discharges have gained popularity in recent decades, due to their unique properties related to plasma chemistry: the energy branching in these discharges is shifted toward excitation of electronically excited species and dissociation by electron impact. The availability of commercially produced nanosecond high-voltage generators, the development of pulse measurement techniques, "ordinariness" of pico- and femtosecond laser measurements [1, 2] have rendered nanosecond plasma no longer exotic, which is currently studied for a wide variety of applications, such as plasma-assisted combustion and detonation [3, 4, 5], plasma-assisted aerodynamics [6, 7], plasma medicine [8] and many more. These applications require an understanding of the spatio-temporal structure of discharge development, often in chemically active mixtures (e.g., in the case of combustion or detonation). Such an understanding can be achieved through plasma modeling, validated against a broad set of experimental data.

The nanosecond discharge in long tubes was first reported in 1893 by J.J. Thomson [9]. He investigated the propagation of a luminous front in a 15-metre glass tube between two vessels with mercury, which were the electrodes and the constructive parts of a mercury pump. The voltage at the high-voltage electrode was a pulse with a calculated decay of about a hundred nanoseconds. Measured using a rotating mirror, the propagation speed of the luminescence front was estimated to be "approximately half the speed of light".

Since then, interest in nanosecond discharges has been renewed every 20-30 years, in correlation with the development of experimental techniques and theoretical approaches. Works on nanosecond discharges of the XX century are reviewed in [10]. Therein, the authors suggest the term "fast ionization wave" (FIW) for nanosecond discharges developing in long tubes (the length of the tube is much bigger than the diameter of the tube) and propagating with a velocity of a few centimeters per nanosecond. The review includes description of dynamics of the propagation of the FIWs generated by high-voltage pulses from a few kilovolts to a few hundreds of kilovolts and duration of a few tens of nanoseconds. Velocities of the FIW propagation in different gases, from nitrogen, air and helium to quite exotic like SF₆, CCl₄ or acetone vapors are presented. Non-local effects in the FIWs front, influence of high-energy electrons on the formation and motion of fast ionization waves are discussed. Theoretical models of fast ionization waves at that time mainly described one-dimensional distribution of the electric field and of current in plasma, special attention being attributed to the run-away electrons in the front of nanosecond discharges at low and moderate pressures.

In the period 1994-2008, a series of papers on the fast ionization waves was published (see for example, [11, 12, 13, 14, 15, 16, 17]), a part of them being summarized in [18, 19]. The papers were devoted to experimental study of the fast ionization waves in so-called kinetic approach when the main interest of study is how to link electrical parameters measured in plasma (the electric field, the electric current, the deposited energy) to the energy branching in the discharge and the efficiency of plasma-chemical processes. The

FIWs were triggered in long tubes by pulses of units-tens of kV at moderate pressures, 0.1-100 Torr.

In particular, it was shown that the peak of high reduced fields [16] in the front of the fast ionization wave, up to several kTd ($1 \text{ Td} = 10^{-17} \text{ V}\cdot\text{cm}^2$), does not exceed two to three nanoseconds in duration. Then the field decreases sharply to hundreds of Td, optimal for excitation of electronically excited levels of atoms and molecules [16, 12]. In the pressure range from units of Torr to tens of Torr, optimal for the development of fast ionisation waves, the peak value of the electric field E increases less than twofold; the reduced electric field E/N decreases almost by an order of magnitude. It was shown, by means of numerical calculations, that at the FIW front, the electron energy distribution function, EEDF, is close to the distribution formed at relaxation of the electron beam in the gas media with predominance of high energy electrons responsible for the homogeneous organisation of the gas [18]. At the same time, the main production of electrons and major energy deposition occur behind the front of the FIW, 5-10 nanoseconds after the peak.

The progress in numerical modeling during the two last decades opened possibilities for more detailed description of nanosecond discharges. Topical review [20] considers sub-nanosecond breakdown in atmospheric pressure gases. The authors of the review claim that, even if numerical simulation of fast pulsed discharges does not reproduce all the complexity of the physical processes involved in the discharge development (i) it provides a much wider set of discharge characteristics comparing to experimental measurements; (ii) it allows easier than in experiment, sensitivity analysis revealing the main factors responsible for the observed phenomena. Finally, it is a synergy of experimental measurements and numerical modeling which provides better understanding of the physical event under study.

As described in the review [10], the first theoretical/numerical investigations of fast ionization waves date back to the late 1970s and early 1980s Soviet era. These studies were based on one-dimensional fluid (hydrodynamic) or long-wavelength approximations and self-similar solutions were obtained for the FIW propagation, which inherently assumes constant properties in the plasma front. In the same review paper, a more general one-dimensional approach based on the telegraph and total current equations is also described which has been used to describe and comprehend several features of the FIW development. Since then, and besides some very interesting theoretical/analytical studies on the solutions of streamer-like planar fronts [21] and FIW propagation in long shielded tubes [22], several one-dimensional models (both kinetic and fluid based) have been used to describe FIWs. Acknowledging the large computational cost of a kinetic description of plasmas based on particles [23, 24] (either using a Monte-Carlo-Collision or Particle In Cell method), which require the solution of the Boltzmann equation to describe the behavior of single particle species, and its dramatic increase in 2D systems despite recent advancements [25], most of FIW numerical studies incorporate the fluid (macroscopic) approximation, where macroscopic quantities such as density, mean velocity and mean energy are used to describe the particle species behaviour

and which correspond to velocity moments of the Boltzmann equation (and relevant closure approximations). The corresponding computational cost is largely reduced compared to kinetic approaches, while the solution of the system of fluid equations (momentum, continuity, energy) can leverage efficient algorithms and discretization schemes on cartesian or unstructured meshes, from the very active Computational Fluid Dynamics (CFD) community. Further assumptions lead to more simplified (and thus computationally efficient) models: neglecting inertia terms in the momentum equation (focusing on non-magnetized plasma), assuming isothermal conditions and collisionality, we derive the drift-diffusion model (see Sec.3 for details), where each species evolution is governed by a single continuity equation in a convection-diffusion-reaction form self-consistently coupled with the electric field through the Poisson equation. Transport and reaction rates depend non-linearly on the reduced electric field under the Local Field Approximation (LFA - 1st order moment model) or the mean electron energy under the Local Mean Energy Approximation (LMEA - 2nd order moment model). Under the LMEA, non-local effects owed to a considerable variation of the electric field over the electron energy relaxation length are accounted for and the model requires the inclusion of an equation for the electron mean energy.

One of the first two-dimensional numerical studies of regular ionization waves in long tubes was performed by Brok et al. [26] in 2003. The authors studied the development of anode directed, DC-excited ionization waves sustained by thermionic emission in moderate pressure (few Torr) Argon and demonstrated the capabilities of fluid modeling to qualitatively capture the breakdown and propagation mechanism, while emphasized the importance of dielectric surface charging. The influence of surface charges and memory effects in such rather slow ionization waves have recently been investigated [27] both experimentally and numerically. Fast ionization waves have been studied self-consistently in dry air and nitrogen [28, 29] but also in Helium [30] and in millimeter and capillary tubes in low pressure N₂ discharges [31, 32, 33, 34], and very recently in short gaps in air and CO₂ [35]. Effects of field emission and relative influence of runaway electrons have been studied with 1D PIC simulations for atmospheric pressure nitrogen [36, 37]. Although this list of numerical works related to FIWs is not exhaustive, it showcases that in the current state of numerical models and High Performance Computing infrastructure, fluid modeling is the typical method for two-dimensional simulations of FIWs. Nevertheless, the computational cost of fluid models is strongly linked on the highly discrepant nature of spatial and temporal timescales of FIWs as well as the dimensions of the simulated discharge region. Accurate, robust and efficient time integration schemes are necessary to account for the extremely different temporal timescales related to electrons and ions drift, assuring that stability (majorly linked to timestep constraints linked to the dielectric relaxation time) is guaranteed. In addition, the development of FIWs in long tubes (several tens of centimeter long as the ones studied in this work), require appropriate meshing in the whole interelectrode gap which renders such 2D simulations extremely time demanding and only possible when parallel computing techniques are efficiently implemented. The

influence of photoionization in gases that are known to efficiently produce photons that can ionize neutral molecules (such as oxygen-nitrogen mixtures) adds up to the numerical challenges.

In this work, we present a detailed 2D axisymmetric self-consistent numerical study of nanosecond moderate pressure discharge in nitrogen propagating in a long tube as a fast ionization wave (FIW). The main goal of this paper is the comparison of self-consistent numerical simulations with the experimental results on FIW propagation obtained within the research group of one of the co-authors and reviewed in [18]. We have deliberately chosen the results which never were a subject of detailed numerical analysis. In particular, the dependence of the FIW velocity and the change in the radial structure of the FIW with pressure depending on the discharge polarity have never been the subject of detailed numerical modeling. Thus, the numerical results are compared with experimental measurements of the FIW propagation velocity, the reduced electric field, the electron density and the $N_2(C^3\Pi_u)$ number density distribution for negative and positive polarities of the applied high voltage pulse. Emphasis is given on both the temporal and spatial development of the discharge, aiming to reveal and understand the particularities of each pulse polarity at different gas pressure inside the 1 - 10 torr range.

The article is structured as follows: in section 2, we provide a brief overview of the experimental setup and findings. In section 3, we present the physical and numerical models used in this study. In section 4, we present the computational case and numerical parameters. In section 5 we present numerical results on electric current, FIW velocity, spatiotemporal distribution of plasma parameters and produced species, comparing them with experimental findings and discussing the results. Last, in section 6, we present the conclusions and propose future directions.

2. A brief information about experimental methods and observed results

A typical experimental scheme is presented in Fig. 1. In the considered experiments, the high-voltage generator (HVG) is always connected to the discharge tube (DT) by a long high-voltage coaxial cable. For the most of experiments with FIWs at moderate (1-50 Torr) pressures, glass or quartz discharge tubes of different lengths (20 to 60 cm) and diameters (1 to 5 cm) are used. Under these conditions, the application of a voltage pulse of 10 to 50 kV amplitude, a few nanosecond rise time and a few tens of nanoseconds FWHM to the high-voltage electrode, initiates an ionization wave which starts always from the high voltage electrode and propagates along the tube. Typically, experiments incorporate a grounded screen linked to the shielding of the high-voltage cable. However, even in the absence of the screen, the ionization wave can propagate as the current closes over the surrounding space. The end load of the discharge tube can be different, often set to zero or infinity; or the low voltage electrode and the grounded screen can be connected to another coaxial cable. Typically, the nanosecond discharge is highly repetitive, and it is possible to accumulate any signal at low frequencies (5-30 Hz)

having a subnanosecond synchronization of the discharge and diagnostics.

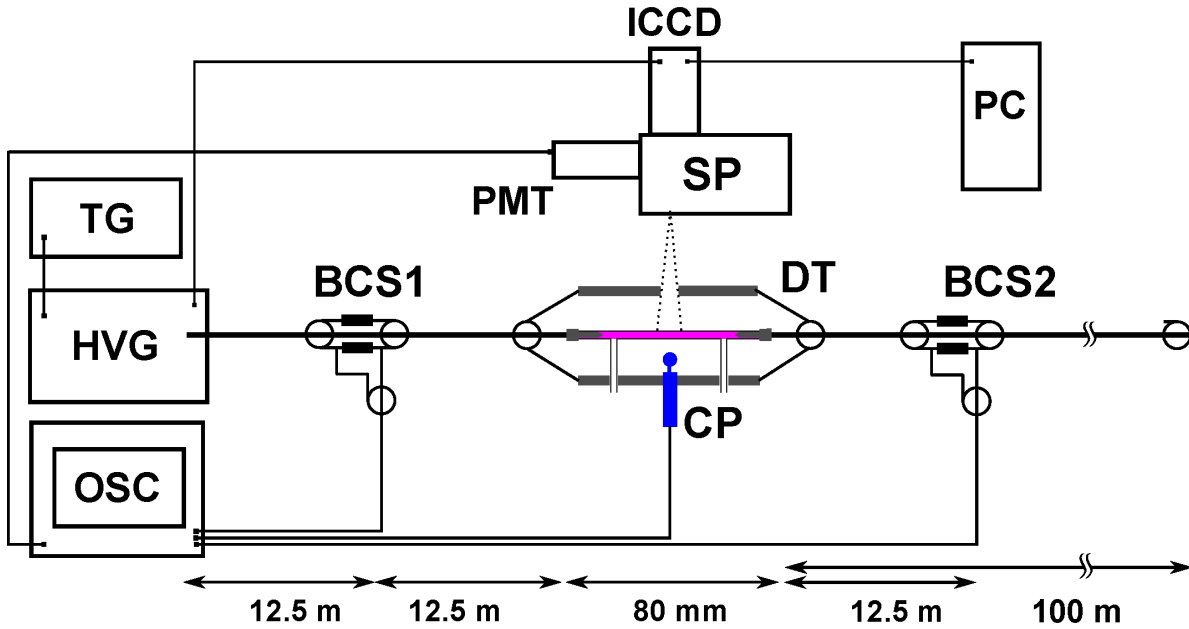


Figure 1: Typical scheme of the experimental setup with the main experimental equipment [38]. The general scheme of the experimental setup with the main experimental equipment. TG is triggering generator, HVG is high voltage generator, OSC is oscilloscope, BCS1 and BCS2 are back current shunts, CP is capacitive probe, DT is discharge tube, PMT is photomultiplier tube, ICCD is intensified charge-coupled device (camera), SP is spectrometer, PC is personal computer.

Spatial structure of the propagating FIW is studied by sub-nanosecond ICCD imaging (0.5-2 ns typical ICCD gates). To control the voltage pulse arriving at the high voltage electrode, to measure the current through plasma and the deposited energy, calibrated custom made back current shunts (BCSs) are used. They are soldered in the grounded shielding of the high voltage cable between the high-voltage generator and the discharge cell so that the incident and reflected from the electrical mismatched load pulses are separated in time. We note here that the voltage on the high-voltage electrode at the moment of the discharge start is doubled comparing to the voltage in the cable as a result of the constructive interference between the incident pulse and the pulse reflected from the discharge tube due to mismatch of the electrical load: 10 kV in the middle of the long cable provides 20 kV at the high-voltage electrode. A description of the back current shunt technique in application to nanosecond discharges can be found in [39].

The velocity of the fast ionization wave and the longitudinal electric field are measured with the help of calibrated custom made capacitive probes (CPs). The electron density is calculated knowing the current, the field and the drift velocity. Time-resolved behavior of electronically excited species is studied using optical emission spectroscopy with the help of a spectrometer linked to the ICCD camera or to the photomultiplier

tube (PMT). All electrical signals are measured by nanosecond oscilloscopes.

A general picture of the development of the nanosecond discharge under mentioned conditions can be summarized as follows: for both negative and positive polarities of the high-voltage pulse, the discharge starts from the high-voltage electrode and propagates with a velocity of a few centimeters per nanosecond [10, 12]. There is a well-defined maximum of the FIW velocity upon pressure. For example, for the voltage amplitude about 10 kV in the cable and the tube diameter of a few centimeters, the maximum velocity is observed around 4 Torr. The position of the maximum shifts to higher pressures as the voltage amplitude increases.

The reduced electric field in the front of the fast ionization wave is high, a few kTd [16]. The duration of this high peak is a few nanoseconds which corresponds, for a given velocity of propagation, to centimeters or even tens of centimeters in length. After the high peak of the electric field, the fields optimal for excitation of electronic levels of molecules and dissociation, a few hundreds of Td, are usually installed. These fields keep constant or only slightly decreasing up to the end of the high voltage pulse. The first high peak of the electric field during the FIW propagation is responsible for the main initial ionization of the gas, resulting in diffuse plasma. In the constant field after the discharge front the electron density can continue to increase, albeit at a significantly reduced rate.

At the dimensions of discharge tubes and the parameters of the high-voltage pulses mentioned above, the specific energy deposited in gas (SED) is typically small, on the order of $10^{-4} - 10^{-3}$ eV/molecule. Typical electron densities are $n_e \sim 10^{12} - 10^{13}$ cm $^{-3}$, providing the ionization degree around $10^{-5} - 10^{-4}$. This means that the recombination time, 1-10 microseconds, is much longer than the duration of the discharge, and the electron density stays constant in time in the discharge and near afterglow [16].

Although the negative and positive polarity FIWs are similar in physical parameters, they differ essentially in their spatial structure. This was observed for air and for nitrogen, as example of ICCD imaging for air is provided by Fig. 2 [14]. The images present raw experimental data, without the inverse Abel transform. The measurements are made for the second positive system of molecular nitrogen, $N_2(C^3\Pi_u) \rightarrow N_2(B^3\Pi_g)$ transition. At these pressures, the life time of $N_2(C^3\Pi_u)$ in air at 1-10 Torr is long, 40 – 20 ns [17], still the pattern of the discharge is clearly seen. At negative polarity, the emission is stronger near the walls, while at positive polarity, the main emission, especially at low pressures, comes from the near-axis region.

In nitrogen, FIWs have a similar space structure, often with more pronounced difference between the axis and the near-wall region. This can be seen from ICCD images in rectangular cross-section double-pulse setup [28] or from $N_2(C^3\Pi_u)$ radial profiles in nanosecond second capillary discharge [40].

The observed difference in the spatial patterns of the FIW for each polarity is not well understood till date. Thus, in the following sections we leverage high-fidelity numerical modeling to explain this difference and explain features of the FIW for both polarities at different gas pressure.

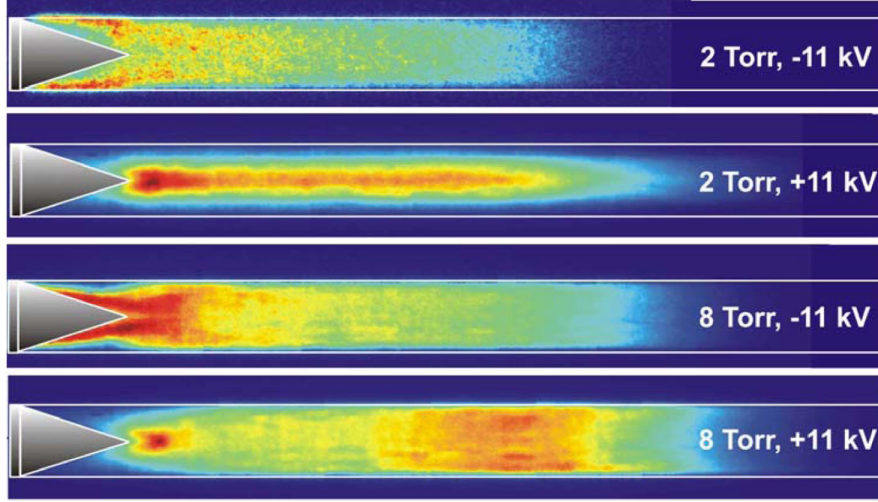


Figure 2: Development of the fast ionization wave in air for different pressures and polarities of the high-voltage pulse. The diameter of the quartz tube is 17.5 mm; the tube length is 50 cm. Emission of the 2+ system of molecular nitrogen. ICCD gate is 1 ns; spectral response is 300–800 nm. Conical high-voltage electrode is on the left-hand side [14].

3. Numerical modeling

We employ a fluid (continuum) description of the plasma which is the core of the physical model used in the computational software COPAIER [41, 42] - a multi-species and multi-temperature plasma fluid solver allowing for self-consistent description of the plasma spatial and temporal evolution (the main author is a co-developer of the solver). Each of the species, s , considered in the pre-defined plasma-gas chemistry is governed by a continuity equation :

$$\frac{\partial n_s}{\partial t} + \vec{\nabla} \cdot \vec{\Gamma}_s = S_s, \quad (1)$$

where S_s is the net rate of production of species s due to chemical reactions and it reads:

$$S_s = \sum_r c_{s,r} R_r + S_{ph}, \quad (2)$$

where $c_{s,r}$ is the net number of particles of species s created or lost in one reaction of type r (so it can be positive or negative). Note that S_{ph} is the photo-ionization source term based on the three-group Helmholtz approximation model [43] (see below).

The species number flux $\vec{\Gamma} = n_s \vec{v}_s$ is given by the momentum balance equation which is approximated by the drift-diffusion equation :

$$\vec{\Gamma}_s = sgn(q_s) n_s \mu_s \vec{E} - \vec{\nabla} (n_s D_s) - n_s \vec{u}, \quad (3)$$

where q is the species charge, μ_s and D_s are the species k mobility and diffusion coefficient respectively, u is the mean mass fluid convection velocity. The electric field is

defined as $\vec{E} = -\nabla\Phi$, with Φ being the electrostatic potential defined by the Poisson's equation

$$\nabla \cdot (\epsilon \nabla \Phi) = -\rho = -\sum_s q_s n_s, \quad (4)$$

where ϵ is the dielectric permittivity.

In Eq. (3) the diffusion coefficient is related to the mobility term by Einstein's relation, $D_s = \mu_s k_B T_s / q$. The rest of transport (mobility μ) and reaction rate coefficients (k) are tabulated with an electric energy dependence under the Local Mean Energy Approximation (LMEA). Under the LMEA, transport and rate coefficients depend on the mean electron energy instead of the electric field (Local Field Approximation - LFA).

To justify our choice of the LMEA over the LFA, we calculate the electron energy relaxation length which can be approximated using[44]:

$$\lambda_e = \sqrt{D_e \tau_e}, \quad (5)$$

where $\tau_e^{-1} = \frac{2m_e}{m_n} \nu + \nu^*$, m_n is the neutral species mass, ν is the elastic collision frequency and ν^* is the inelastic collision frequency. In our conditions, we estimate λ_e in the 5-10 mm range. The discharge gap, L , is 60 cm and most importantly, the FIW front (as we'll see below) presents strong gradients of the electric field in length scales that are millimetric, which indicates that non-local effects are important and the validity [45] of the Local Field Approximation (LFA) and local field equilibrium is violated.

The mean electron temperature can be obtained by the electron energy conservation given as :

$$\frac{\partial n_\epsilon}{\partial t} + \vec{\nabla} \cdot \vec{\Gamma}_\epsilon = S_\epsilon, \quad (6)$$

where $n_\epsilon = n_e \epsilon$ is the electron energy density and ϵ is the electron mean energy which by assuming that is a results mainly from random motion relates to the electron mean temperature by $k_B T_e = 2/3 \epsilon$.

The electron energy flux reads :

$$\vec{\Gamma}_\epsilon = \frac{5}{3} \epsilon \vec{\Gamma}_e + \vec{q} \quad (7)$$

The heat flux, \vec{q} is assumed proportional to the gradient of the electron mean energy :

$$\vec{q} = -\frac{5}{3} n_e D_e \nabla \epsilon \quad (8)$$

The source term, S_ϵ includes heating by the electric field (electron Joule heating) and energy losses in inelastic and elastic collisions as:

$$S_\epsilon = -e \vec{\Gamma}_e \cdot \vec{E} - \sum_{i=1}^{N_{react}} \Delta E_i r_i - \frac{3}{2} k_b n_e \frac{2m_e}{m_g} (T_e - T_g) \nu_m \quad (9)$$

The first term in the right hand side corresponds to the electron Joule heating term. The second term is the sum for each electron impact reaction, i , of the inelastic electron

energy loss, where ΔE_i is the energy threshold (thermal energy loss) in reaction i and r_i is the rate of progress. The summation is performed over the total number of gas-phase reactions, N_{react} . The last term, corresponds to the energy loss due to elastic collisions which can also be approximated with an effective rate coefficient and integrated directly to the inelastic energy loss term. In this last term, ν_m is the electron momentum-transfer frequency, T_g is the gas density, m_g is the heavy species particle mass, m_e is the electron particle mass.

The density of the background species is given by the ideal gas law :

$$p = \sum n_s k_B T_s \quad (10)$$

Surface charge accumulation on dielectric surfaces is taken into account by assuming that particles stick to the dielectric surface and no diffusion occurs. Thus the surface charge is given by:

$$\sigma = \int \vec{j} \cdot \vec{n} dt, \quad (11)$$

where the plasma current density reads :

$$\vec{j} = \sum_s q_s \vec{\Gamma}_s \quad (12)$$

Lastly, we include a photoionization model involving the solution of three Helmholtz type equations [43] in the form:

$$\nabla^2 S_{ph,j} - (\lambda_j p)^2 = -A_j p^2 I_{ion} \quad (13)$$

for $j = 1, 3$, where $S_{ph,j}$ is the photoionization source term in m^3/s for equations $j = 1, 3$, the gas mixture pressure is denoted as p and I_{ion} is the ionization rate. The total photoionization source term is then simply given by:

$$S_{ph} = \sum_{j=1}^3 S_{ph,j}. \quad (14)$$

The six coefficients, λ_j and A_j are exponentially fitting parameters for the photon propagator function which is given as:

$$\frac{\Phi_0}{p}(pr) = (pr) \sum_{j=1}^3 A_j e^{\lambda_j pr} \quad (15)$$

The function $\frac{\Phi_0}{p}(pr)$ has been calculated for pure nitrogen in low pressure using the PHOTOPiC software [46, 47]. The fitting coefficients have been calculated by minimizing an ordinary least square cost function and are presented in Table 1. Although photoionization occurs more efficiently when small amounts of oxygen are present in the gas as UV photons mainly produced from radiative decay of nitrogen excited species ionize oxygen molecules, the mechanism is present in pure nitrogen [48] also (although poorly understood and studied), and our numerical results showed that its inclusion is important for a correct representation of the FIW propagation speed.

A detailed description of several numerical schemes available in the COPAIER solver can be found in [42, 41, 49]. Here we summarize the main features used in this

Table 1: Fitting coefficients for the photoionization three-group Helmholtz model

j	A_j	λ_j
1	4.6657×10^{-5}	0.51102
2	3.8146×10^{-4}	0.951
3	7.4994×10^{-4}	4.2468

A_j in cm⁻²Torr⁻²
λ_j in cm⁻¹Torr⁻¹

specific study. A finite volume approach is used to solve the drift-diffusion equations. The Scharfetter-Gummel flux scheme [50] is used here to discretize the convection-diffusion operator of species continuity equations. Temporal integration for the species system of continuity equations is performed via an implicit time-marching algorithm based on the Gauss-Seidel technique [51].

In Eqs (6) and (9), the evaluation of the energy loss source term explicitly can lead to non-physical oscillations that can damage the stability of the whole system. In order to circumvent this issue, an implicit treatment of the joule heating source terms has been adopted based on [52]. The energy loss source term is treated fully implicitly as well as all electron-impact reaction source terms involving neutral species as reactants. The Finite Element Method has been used to solve the Poisson and Helmholtz equations, with a P1-Finite Element formulation. A semi-implicit formulation for the Poisson equation, similar to the one proposed in [53] has been implemented, allowing to circumvent the dielectric relaxation timestep constraints. The numerical solver is parallelized based on the MPI paradigm and a non-overlapping domain decomposition method.

3.1. Plasma chemistry model

We choose to use a reduced N₂-plasma chemistry, where nine (9) modeled species are included, consisting of electrons, positive N₂⁺ and N₄⁺ ions, neutral N₂ molecules as well as the following excited states: N₂(A³Σ_u⁺), N₂(B³Π_g), N₂(C³Π_u), N₂(a¹Σ_u). Sixteen (16) chemical reactions (in addition to photoionization) are taken into account which and listed in Table 2. Transport coefficients and reaction rates for R1-R6 and R6-R7 have been calculated using the two-term Boltzmann solver, BOLSIG+ [54] including electron-electron, electron-ion and superelastic collisions and under the exponential growth (PT) model. We assume a gas composition of 100% N₂. The ionization degree is assumed 10⁻⁵, the electron density 10¹⁸ m⁻³ and the gas temperature 300 K. Cross-sections for N₂ used as inputs in BOLSIG+ have been taken from the Phelps database [55] and includes 26 electron-neutral scattering cross sections describing dissociative attachment, effective

momentum transfer, ionization, rotational, electronic and vibrational excitation. The direct electron-impact ionization (15.6 eV) cross section dataset has been extended to high electron energies based on [56, 57]. To include associated electron impact energy losses, all excited (rotationally, vibrationally in different levels and electronically) species which are not tracked have been lumped to a single species, denoted as $N_2(\text{lump})$ which is also not tracked (assumed as N_2). The rate coefficient for R15 is then calculated as follows: we equate the sum of contributions of all these untracked reactions to the inelastic power loss term, with the loss of the fictitious lumped reaction (R15). Assuming that the energy threshold for R15 is 1 eV, we get the following formula for the rate coefficient:

$$k_{lump} = \sum_{i=1}^n (\Delta E_i k_i), \quad (16)$$

where ΔE_i and k_i are the energy threshold and rate coefficient for reaction i , and n are the total number of excitation reactions (not tracked). N atoms are not tracked (assumed as $0.5 N_2$ in R8) as well as vibrationally excited N_2 states (assumed in ground state of N_2). This reduced chemistry set is of course rather simplified but provides a good balance between accuracy and required computational time, allowing us to capture the main features of the FIW dynamics, while stabilizing the numerical algorithm under the LEA scheme, by incorporating the main electron energy loss mechanisms.

Reduced ion mobilities for N_2^+ and N_4^+ (in N_2) have been taken from LxCAT swarm data (Phelps and Viehland databases [55, 58]). Constant (reduced) diffusion coefficient of $1.98 \times 10^{-5} \text{ m}^2/\text{s}$ was assumed for all neutral species. We neglect gas flow dynamics as their timescales are much larger than the simulation time-scales. The gas temperature (T_g) is assumed constant at 300 K. This is a good approximation on the nanosecond FIW propagation timescales, as (i) we mainly consider the FIW front propagation, at this time scale the heating can be neglected; (ii) the specific energy delivered to plasma is low.

Electrons and positive N_2^+ and N_4^+ ions are initialized with a number density of $2 \times 10^{14} \text{ m}^{-3}$ and 10^{14} m^{-3} respectively, rest of neutral species with a density of 10^3 m^{-3} . This roughly corresponds to levels of residual charges from the repetitive nanosecond pulses of 10 Hz.

A floor density of 10^9 m^{-3} is used for all charged species to emulate the effects of cosmic rays induced, background ionization. These values also correspond to the floor density for each species respectively. The secondary electron emission (SEE) coefficient for the electrode boundary is set to 10^{-3} while for the dielectric rods and barrier to 1×10^{-2} . The influence of these parameters on the discharge evolution falls outside the scope of this work.

4. The case under study, computational and initial parameters

The computationally domain mimics the experimental setup: a 60 cm long quartz tube is used with inner diameter, 17.5 mm, outer diameter, 21.5 mm, with metallic electrodes

Table 2: Chemical reaction model used in the simulations.

Reaction	Rate coefficient	Comment - Source
R1: $e + N_2 \rightarrow N_2^+ + 2e$	$f(E)$	$\Delta E_i = 15.6$ eV, Ref. [55] ^a
R2: $e + N_2 \rightarrow N_2^+ + 2e$	$f(E)$	$\Delta E_i = 18.8$ eV $N_2^+(B^2\Sigma_u^+)$ excitation, Ref. [55] ^a
R3: $e + N_2 \rightarrow N_2(A) + e$	$f(E)$	$v0-4$, Ref. [55] ^a
R4: $e + N_2 \rightarrow N_2(B) + e$	$f(E)$	Ref. [55] ^a
R5: $e + N_2 \rightarrow N_2(C) + e$	$f(E)$	Ref. [55] ^a
R6: $e + N_2 \rightarrow N_2(a') + e$	$f(E)$	Ref. [55] ^a
R7: $e + N_4^+ \rightarrow N_2 + N_2$	$2 \times 10^{-6}(300/T_e)^{0.5}$	Ref. [59] ^b
R8: $e + N_2^+ \rightarrow N + N(2D)$	$2 \times 10^{-7}(300/T_e)^{0.5}$	N atoms not tracked (assumed 0.5 N_2) , Ref. [59] ^a
R9: $N_2(C) \rightarrow N_2(B) + h\nu$	2.45×10^7	Ref. [60] ^d
R10: $N_2(C) + N_2 \rightarrow N_2(a') + N_2(v)$	1×10^{-11}	Vib. state not tracked (assumed N_2) , Ref. [59] ^b
R11: $N_2(B) + N_2 \rightarrow N_2(A) + N_2(v)$	1×10^{-11}	Vib. state not tracked (assumed N_2), Ref. [59] ^b
R12: $N_2(a') + N_2 \rightarrow N_2(v) + N_2(v)$	2×10^{-13}	Vib. state not tracked (assumed N_2), Ref. [59] ^b
R13: $N_2(A) + N_2(A) \rightarrow N_2(C) + N_2(v)$	1.6×10^{-10}	Vib. state not tracked (assumed N_2), Ref. [59] ^b
R14: $N_2(A) + N_2(A) \rightarrow N_2(B) + N_2(v)$	7.7×10^{-11}	Vib. state not tracked (assumed N_2), Ref. [59] ^b
R15: $e + N_2 \rightarrow N_2 + e$	$f(E)$	Lumped state - see text, Ref. [55] ^a
R16: $N_2^+ + 2N_2 \rightarrow N_4^+ + N_2$	5×10^{-29}	Ref. [59] ^c

^a Bolsig+.^b Units of cm^3/s . T_e in K.^c Units of cm^6/s .^d Units of $1/\text{s}$.

Table 3: Geometrical and operational conditions for the simulations.

HV electrode half-angle	$\theta = 15$ degrees
Discharge tube internal diameter	$D_1 = 17.6$ mm
Discharge tube external diameter	$D_2 = 21.6$ mm
Shielding cage diameter	$D_3 = 60$ mm
Inter-electrode gap	$L = 60$ cm
Relative permittivity of dielectric	3.2

at the ends of the tube. The high-voltage (HV) electrode has a 25 mm long conical shape with a cone angle of 30 degree. The low-voltage (grounded) electrode is plate-shaped. Thus, while the inter-electrode gap, L , equals the tube's length (60 cm), the axial distance between the HV electrode's apex and the ground electrode is approx. 56.7 cm. The tube is surrounded by a cylindrical, grounded, metallic shield of inner diameter 60 mm. Fig. 3 presents an illustration of the computational domain and relevant dimensions.

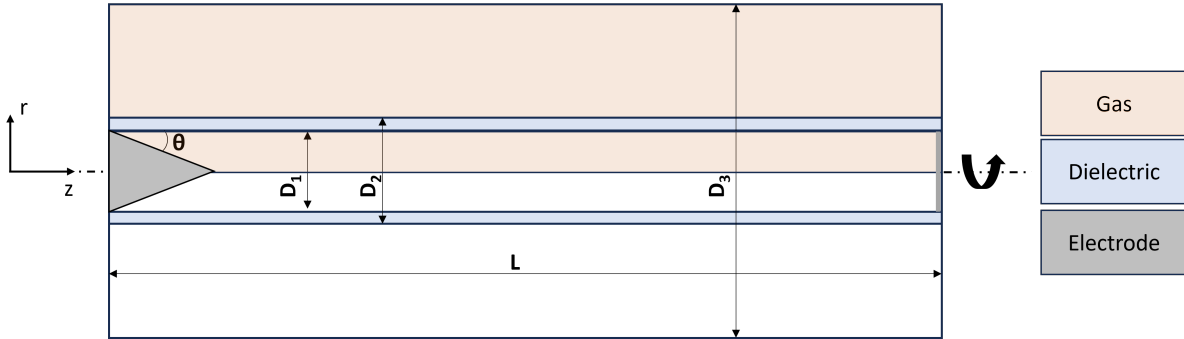


Figure 3: Illustrative graph of the discharge tube. The axisymmetric computational (CPU) domain corresponds to the upper half. Dimensions not in scale.

In the experiments, a pulse of 13.5 kV amplitude, 25 ns duration at half width and 6 ns rise time was supplied from a high-voltage generator with a 40 Hz repetition frequency. In the simulations, we apply a similar waveform (one pulse) but with amplitude of 27 kV to emulate the constructive interference between the forward and backward propagating pulses. In Table 3, we summarize the geometrical and operational conditions for the simulations (see also Fig. 3).

The computational mesh is an unstructured one, created in the Gmsh [61] software, properly refined near the electrodes and near the dielectric surface. It consists of 589.445 triangular cells. The minimum cell size is approximately $10 \mu\text{m}$ at the “boundary layer” zone near the electrodes and adjacent to the dielectric surface in order to resolve all plasma-related aspects such as sheaths and cathode layer formation. The computational mesh at the region around the HV electrode tip is shown in Fig. 4. The domain has

been decomposed in 32 sub-domains and the calculations were run on a local HPC workstation (Dell PowerEdge R7515) over 32 computational units (AMD EPYC 7352), leveraging MPI-parallelism.

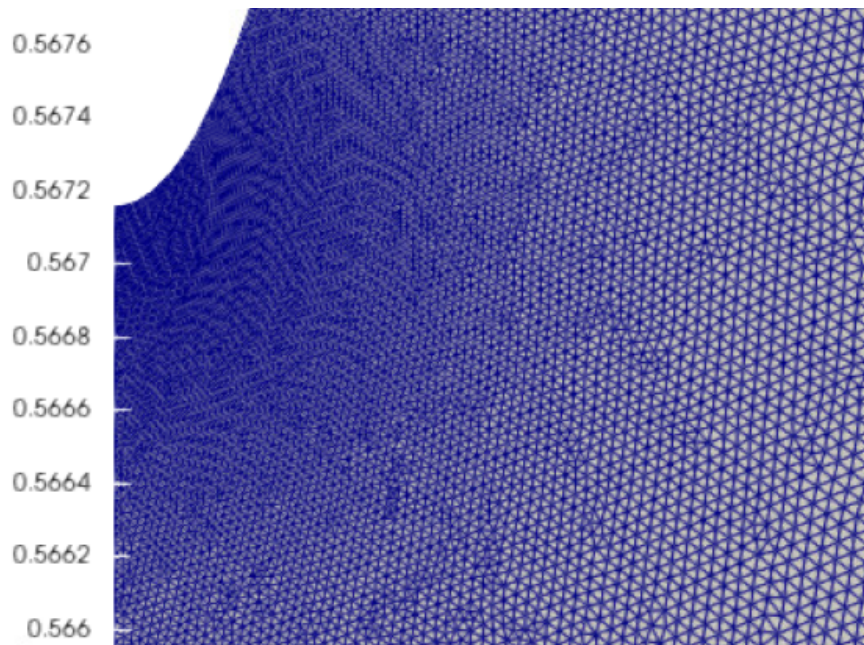


Figure 4: Unstructured mesh refinement near the HV electrode tip. Similar refined regions are used near the dielectric surface and both electrode surfaces.

5. Results and discussion

Fig. 5 presents an example of the synchronized voltage and calculated current waveforms for nitrogen, 10 Torr pressure. The voltage waveform is the initial data of the problem, while the current waveform is calculated during the simulations. Different shapes of the current are observed for negative and positive polarity: the current behaviour at negative polarity is similar to the surface discharge, when two peaks of different polarity are observed at rising front and falling edge of the high voltage pulse; the current at positive polarity is high after the front. Typical values for current for both polarities are tens of A.

5.1. FIW velocity

Velocity, measured as a gradient of the electric charge along the discharge tube [62] and maximum velocity calculated from the propagating front and the position of maximum total charge (in absolute value), are presented together for negative and positive polarities in Fig. 6. Increase of the FIW velocity up to a few Torr and then decrease is confirmed by results of the modeling. A reasonable agreement between the calculated and the measured absolute values of the velocity for negative polarity and a

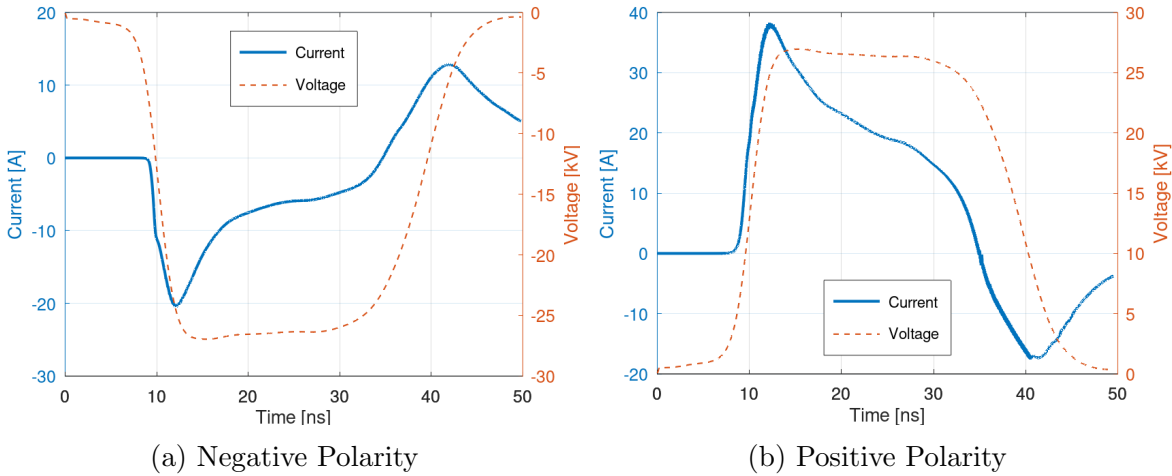


Figure 5: Experimental voltage waveforms (orange dashed curves), used as applied voltage in the numerical solver; calculated current through the discharge cell, (solid blue curves). Measurements are made by capacitive probe; the velocity is calculated by the 0.5 level from the amplitude of the signal. Nitrogen, pressure 10 Torr.

quantitative agreement for positive polarity are clearly seen. Typical values of the FIW propagation speed along the tube are 2 – 4 cm per nanosecond.

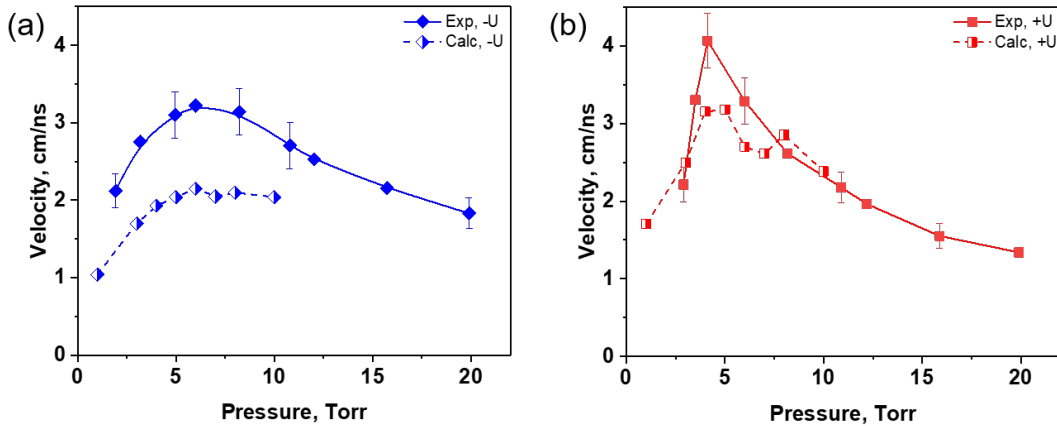


Figure 6: Experimental [62] (filled symbols) and calculated (half-filled symbols) velocities of the fast ionization wave (FIW) propagation. Nitrogen, (a) negative polarity; (b) positive polarity.

We note here that (i) at negative polarity, a double structure of the ionization wave, with a lower amplitude (“a precursor”) has been observed [12]; (ii) the calculated values have been extracted only from the saved output data from the simulations and not at every time step (to reduce the generated data and due to storage limitations) and as such, the maximum velocities reported here might deviate slightly from the reality. This

fact also can explain the small jump observed at 8 Torr under positive polarity.

In any case, the observed trends and orders of magnitude are quite satisfactory when compared with the experimental findings. We also need to emphasize that the calculated velocities represent the maximum velocity of the FIW: under most of the conditions studied here, the calculated FIW velocity quickly increases to the maximum value and then slowly decays during its propagation, thus the velocity is non-constant.

The optimum pressure for development of a nanosecond discharge for given amplitude of the high-voltage pulse, nitrogen pressure and the discharge tube diameter is about 5 Torr. The trends observed in the numerical results (which are in good agreement with the experimental data) suggest a rather complex dependence of the propagation speed on the plasma structure and the discharge main parameters (electric field, plasma density etc). As we will see in the following sections, under different polarities and different background pressures, the plasma development and properties differ significantly which renders a straight-forward explanation of the FIW speed behavior difficult to obtain. Nevertheless, we can extract some interesting information based on the theoretical work [22]. Therein, the authors provide analytical self-similar solutions of the (averaged over the cross-section) problem of high-speed ionizing wave (FIW) propagation in long shielded tubes. A rather simple equation is then provided to describe the FIW speed:

$$v_{FIW} = \frac{\phi_f \nu(T_e)}{E_0 e} \quad (17)$$

In the above formula, ϕ_f , E_0 and $\nu(T_e)$ are the electrical potential, the maximum of the electric field and the ionization frequency at the FIW front, respectively, while e is the base of the natural logarithm. Note that we have used the electron temperature dependence of the ionization frequency, $\nu(T_e)$, due to our LEA modeling approach. All these parameters are direct outputs of our simulations and can be used to plot the analytical dependence of the FIW speed over pressure for both polarities. This is shown in Fig. 7, which demonstrates a good qualitative agreement with the calculated values from the simulations.

Our calculations (see following sections for details) show that, for a negative polarity FIW, the potential ϕ_f and the maximum electric field at the front, E_0 , increase monotonically with pressure by nearly an order of magnitude, while their ratio remains constant. Consequently, the speed of the FIW front is approximately proportional to the ionization frequency $\nu(T_e)$. Will note that, despite their increase, the potential and electric field remain approximately half of the corresponding values observed for positive polarity. This behavior reflects the fact that, under a negative polarity pulse, electrons propagate ahead of the FIW front region. With this pre-ionization, the FIW can propagate even in a relatively low field.

For positive polarity FIW, the electrons more backward, to the bulk of plasma. Both the potential ϕ_f and maximum electric field at the front E_0 remain almost constant over the studied pressure range. Electric field being constant, the reduced electric field E/N

drops by an order of magnitude between 1 and 10 Torr. In the calculations, a sharp drop of T_e is observed when pressure increases from 1 to 10 Torr. As a result, at low pressures, very high T_e and low collision frequencies the ionization efficiency, the electron density and the FIW speed are low, the E/N values are higher than the most efficient ones for the ionization. At high pressures, on the right decaying branch of v_{FIW} , the E/N values are lower than the most efficient ones for the ionization, and the maximum value of v_{FIW} is reached in between, corresponding to maximum ionization.

For a positive polarity FIW, electrons move backward, to the plasma bulk. Both the potential ϕ_f and the maximum electric field at the front, E_0 , remain nearly constant over the studied pressure range. With the electric field being constant, the reduced electric field E/N decreases by an order of magnitude between 1 and 10 Torr. The calculations reveal a sharp drop in T_e with pressure increase. Consequently, at low pressures, ionization efficiency, electron density, and FIW speed remain low, and E/N exceeds the optimal values for ionization. At high pressures, on the right decaying branch of v_{FIW} , E/N falls below the optimal one for ionization, with the maximum value of v_{FIW} occurring at an intermediate pressure.

So for both polarities of the high-voltage pulse, the main parameter influencing the FIW propagation speed according to formula (17) is the ionization frequency $\nu(T_e)$ at the FIW front. Discrepancies in the absolute values of the FIW speed between the analytical formula and results of calculations (see Fig. 6) can be attributed to the choice of values at the FIW front and limitations of the self-similar analytical approach.

The electron density as a function of pressure exhibits a maximum at approximately the same pressure as the FIW front speed. On the right decaying branch of v_{FIW} , the conditions are optimal for dissociation through the excitation of molecular electronic levels, with the dissociation degree reaching its maximum at a higher pressure than the FIW speed maximum. Experimental data on electron density measured via microwave interferometry [63] and O_3 production measured via UV absorption [64] strongly support this reasoning regarding the dependence of discharge parameters on pressure and the relative positions of the maxima.

To trace the most characteristic interval of the FIW propagation and retrieve information on discharge aspects that influence the FIW speed for both polarities, simulation results are presented below for 1, 5 and 10 Torr.

5.2. Spatiotemporal distribution of electric field, electron temperature, charged species densities and density of $N_2(C^3\Pi_u)$.

Calculated spatiotemporal distribution, represented as $x-t$ diagrams, of the electron and ion densities, density of $N_2(C^3\Pi_u)$, the longitudinal component of the reduced electric field $|E_z|/N_g$ and the electron temperature T_e for negative and positive polarities of the high-voltage pulse are presented and discussed in this section. All values are taken on the axis of the discharge, at $r = 0$. The point $(Z; t) = (0; 0)$ corresponds to the high-voltage electrode, $Z = 60$ cm corresponds to the low-voltage electrode, and $t > 30$ ns

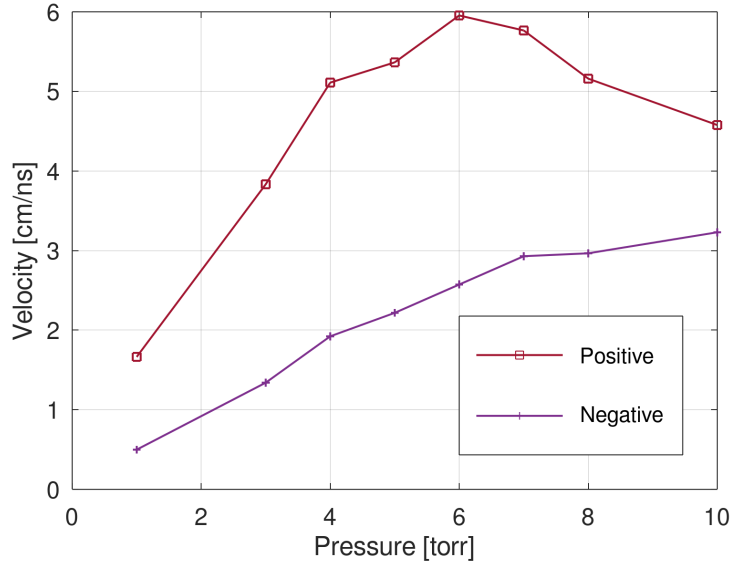


Figure 7: Analytical velocities (Eq. 17) of the fast ionization wave (FIW) for positive and negative polarity versus pressure.

corresponds to the falling edge of the high-voltage pulse. Note that for visualization purposes, the graphs of electron temperature and reduced electric field are excluding the sheath zones near the electrodes (where very high values are observed). Similarly, minimum values of E/N , T_e and species density limited to 0.1 Td, 0.1 eV and 10^{14} m^{-3} respectively, also for visualization purposes, while maximum values for species densities are limited to 10^{20} m^{-3} (only in the cases of positive polarity such limitation acts in the near-electrode regions).

5.2.1. Negative polarity Figures 8, 9, 10 show the spatiotemporal behavior for negative polarity discharge at gas pressure $P = 1, 5$ and 10 Torr respectively. The discharge onset and formation of high electron density is clearly seen in the interval 5-10 ns, depending on pressure. The discharge velocity is higher at the beginning, decelerating as the FIW propagates along the tube. This is a distinctive feature of the negative polarity discharge, which is more pronounced for low pressures: for example, for $P = 5$ torr, the discharge velocity gradually decreases from 2 cm/ns (at 13.64 ns) to 0.68 cm/ns (at 32.1 ns) as the FIW develops in the gap.

The front of the fast ionization wave, or a region with a high electric field, lasts a few nanoseconds, in agreement with experimental observations. The duration of this high peak of E-field is a function of pressure, decreasing from 5-10 ns at 1 Torr to 1-2 ns at 10 Torr. At 1 Torr, a plasma sheath with thickness of approx. 0.6 cm is clearly visible near the left electrode (at distance $z=0$). The electron density produces mainly in the FIW front. The front represents a gradient of both electron and N_2^+ ions, with a length of approximately 4 cm. Behind the FIW front, the quasi-neutral plasma body sustains

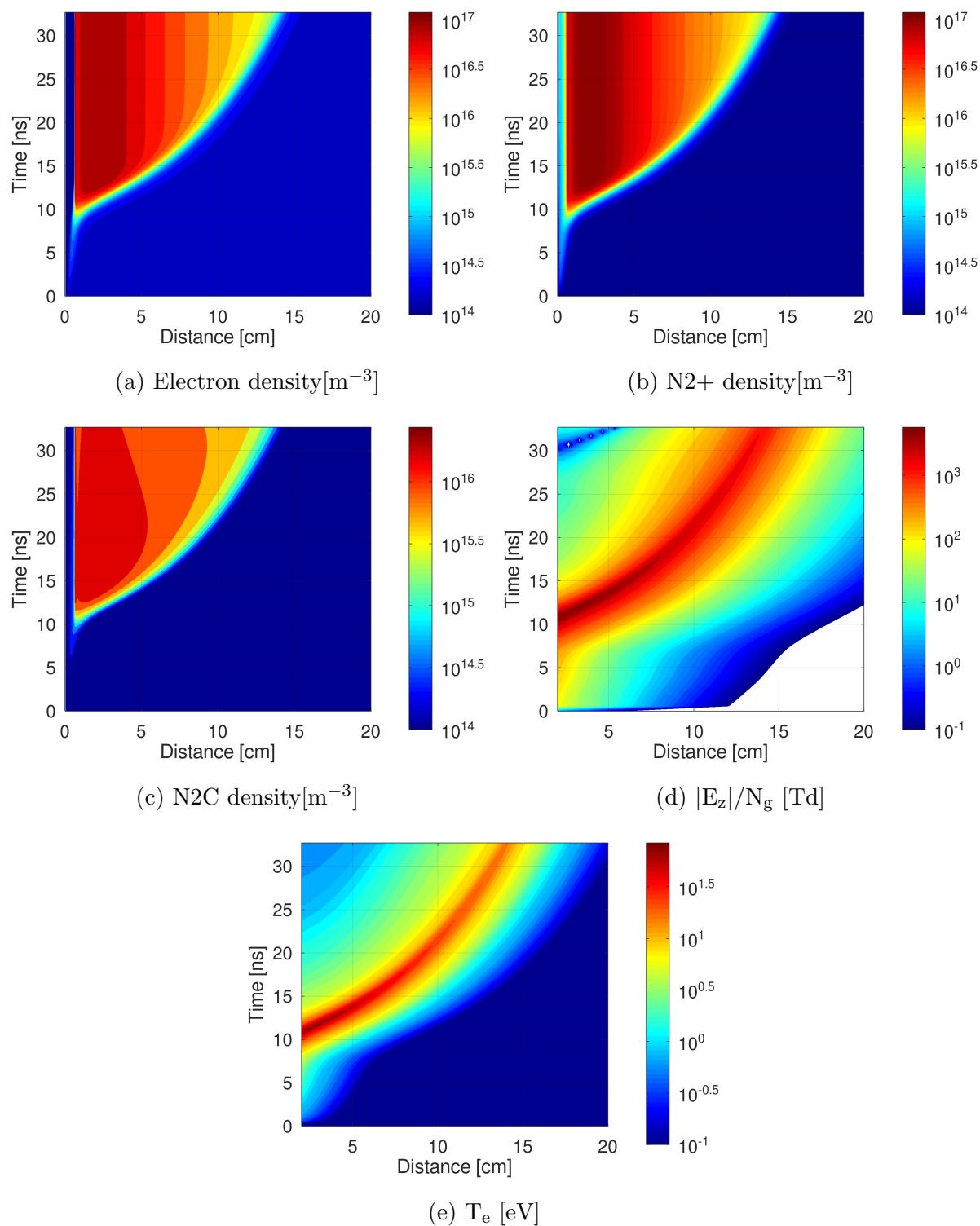


Figure 8: Negative polarity at 1 Torr: Axial distance vs time contour plot of electron, N_2^+ , $\text{N}_2(\text{C}^3\Pi_u)$ species density [m^{-3}], axial component of reduced electric field magnitude [Td] and electron temperature [eV] at $r=0$. All plots in log-scale.

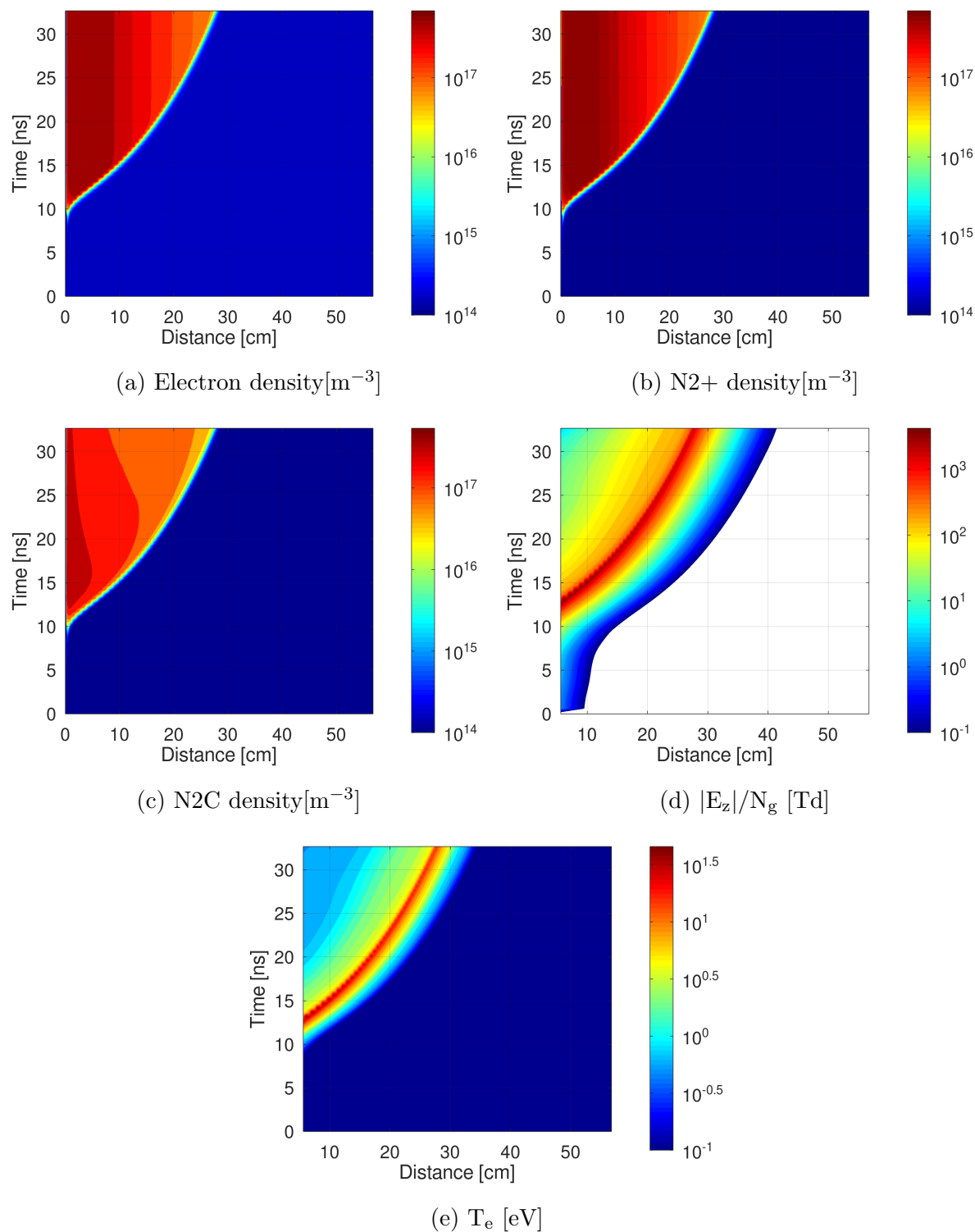


Figure 9: Negative polarity at 5 Torr: Axial distance vs time contour plot of electron, N_2^+ , $\text{N}_2(\text{C}^3\Pi_u)$ species density [m^{-3}], axial component of reduced electric field magnitude [Td] and electron temperature [eV] at $r=0$. All plots in log-scale.

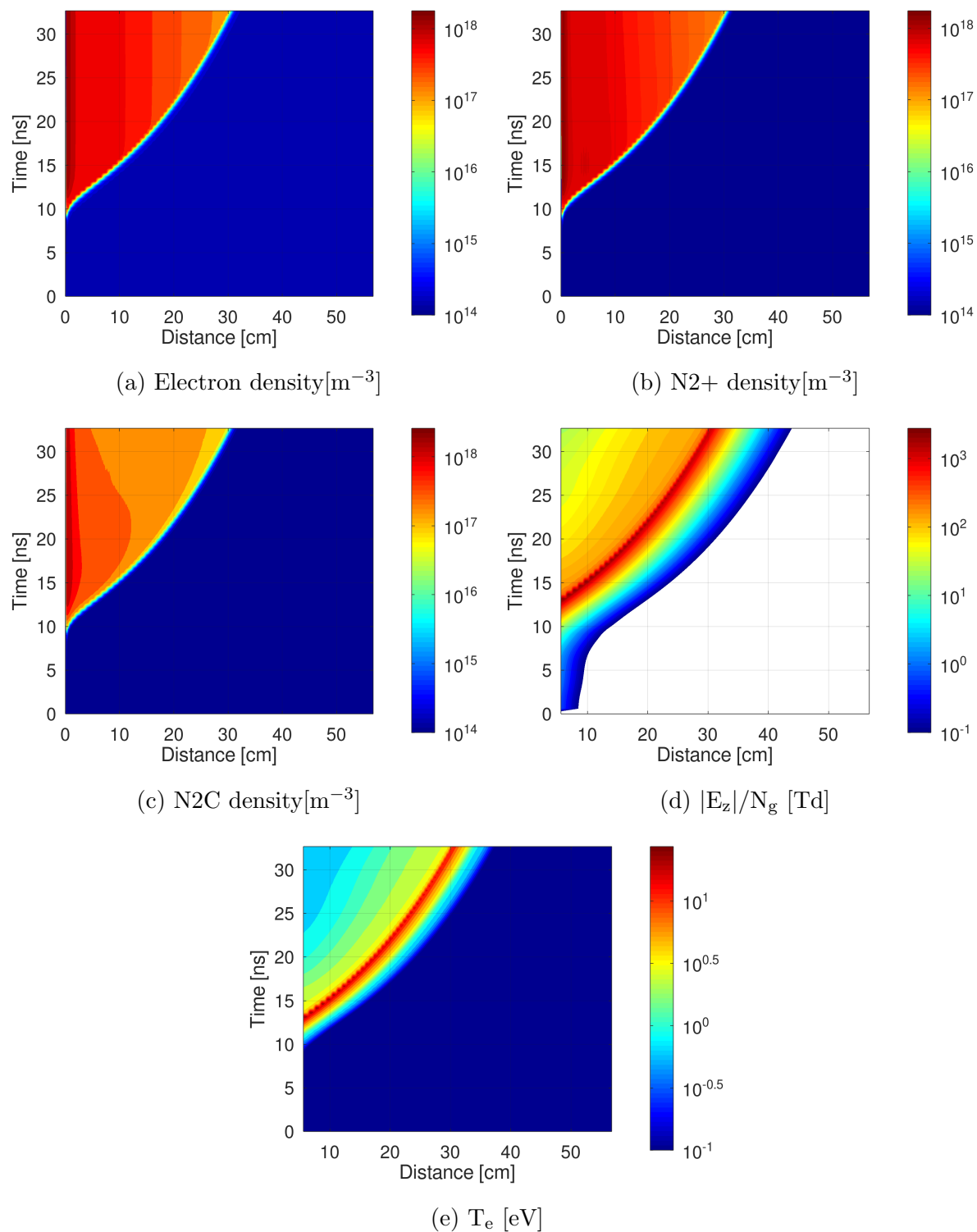


Figure 10: Negative polarity at 10 Torr: Axial distance vs time contour plot of electron, N_2^+ , $\text{N}_2(\text{C}^3\Pi_u)$ species density [m^{-3}], axial component of reduced electric field magnitude [Td] and electron temperature [eV] at $r=0$. All plots in log-scale.

electron and N_2^+ densities in the order of $10^{11} - 10^{12} \text{ cm}^{-3}$. Electron-ion recombination for such a period of time can be disregarded and the decrease of the level excitation rate is caused by a decrease of the electron energy. Hence, the electron density monotonically builds up during the impulse and becomes stationary. Behaviour of density of N_2^+ ions repeats the behaviour of electrons; the densities of other ions are much lower.

In the plasma bulk, increasing electron density, and still high despite the decreasing electric fields, lead to efficient excitation of $N_2(C^3\Pi_u)$ -state, producing a major part of optical emission of the nanosecond moderate pressure discharges in nitrogen. The delay between the FIW front and $N_2(C^3\Pi_u)$ excitation is clearly seen. The density of $N_2(C^3\Pi_u)$ -state inside the plasma bulk is in the order of 10^{11} cm^{-3} . The picture corresponds completely to experimental observations of paper [16] describing population of nitrogen molecule electron states and structure of the fast ionization wave.

The calculated reduced electric field and electron temperature inside the plasma bulk are in the order of $10 - 100 \text{ Td}$ and $1 - 5 \text{ eV}$ while the FIW front sustains quite high fields in the order of 1000 Td and higher, with electron temperatures in the $10 - 30 \text{ eV}$ range. Such high values of E/N are in agreement with several modeling results [33, 31, 32].

5.2.2. Positive polarity Figures 11,12,13 show $x - t$ diagrams of the electron and ion densities, density of $N_2(C^3\Pi_u)$, the longitudinal component of the reduced electric field $|E_z|/N_g$ and the electron temperature T_e for positive polarity of the high-voltage pulse. As everywhere in this work, the discharge is in nitrogen.

Similar to the negative polarity discharge, the discharge starts from the high-voltage electrode at approximately 8 ns. Differently from the negative polarity, the FIW propagates at an almost constant velocity, especially for lower pressures. Similar to the negative polarity, the FIW front presents a gradient of both electron and N_2^+ ions, with a length of approximately 4 cm. Behind the FIW front, the quasi-neutral plasma body sustains electron and N_2^+ densities in the order of $10^{12} - 10^{13} \text{ cm}^{-3}$, with higher values observed at lower pressure. $N_2(C^3\Pi_u)$ distribution follows the FIW development, but densities inside the plasma bulk are higher and in the order of 10^{12} cm^{-3} .

At moderate and higher pressure, and similar to the negative polarity discharge, $N_2(C^3\Pi_u)$ front presents a weaker gradient with a length of more than 10 cm, owed to a convolution of increasing electron density and decreasing electric field. Even if, similar to the negative polarity discharge, the electric field in the FIW front is much higher than behind the front, the difference between the field in the front and after the front is much higher for positive polarity. The calculated reduced electric field and electron temperature inside the plasma bulk are similar to negative polarity (in the order of $10 - 100 \text{ Td}$ and $1 - 5 \text{ eV}$ respectively) but the FIW front sustains substantial higher fields in the order of 10000 Td , resulting to electron temperatures around and even higher than 100 eV . As mentioned also before, such high values of E/N are consistent with several modeling results [31, 32, 33]. Without going into details, will note that so high values of electron energy observed in numerical simulation in the FIW front, may

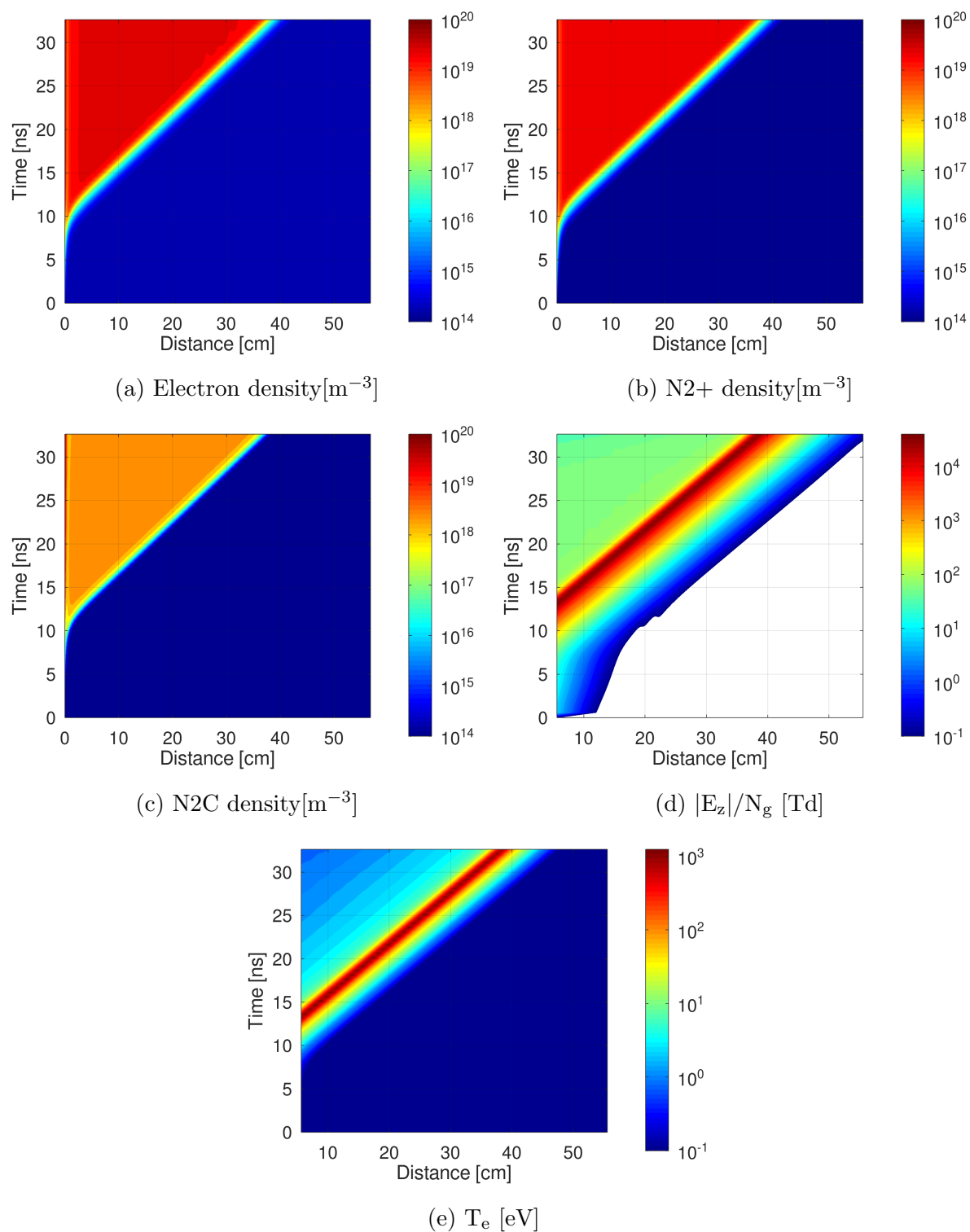


Figure 11: Positive polarity at 1 Torr: Axial distance-time contour plot of electron, N_2^+ , $\text{N}_2(\text{C}^3\Pi_u)$ species density [m^{-3}], axial component of reduced electric field magnitude [Td] and electron temperature [eV] at $r=0$. All plots in log-scale.

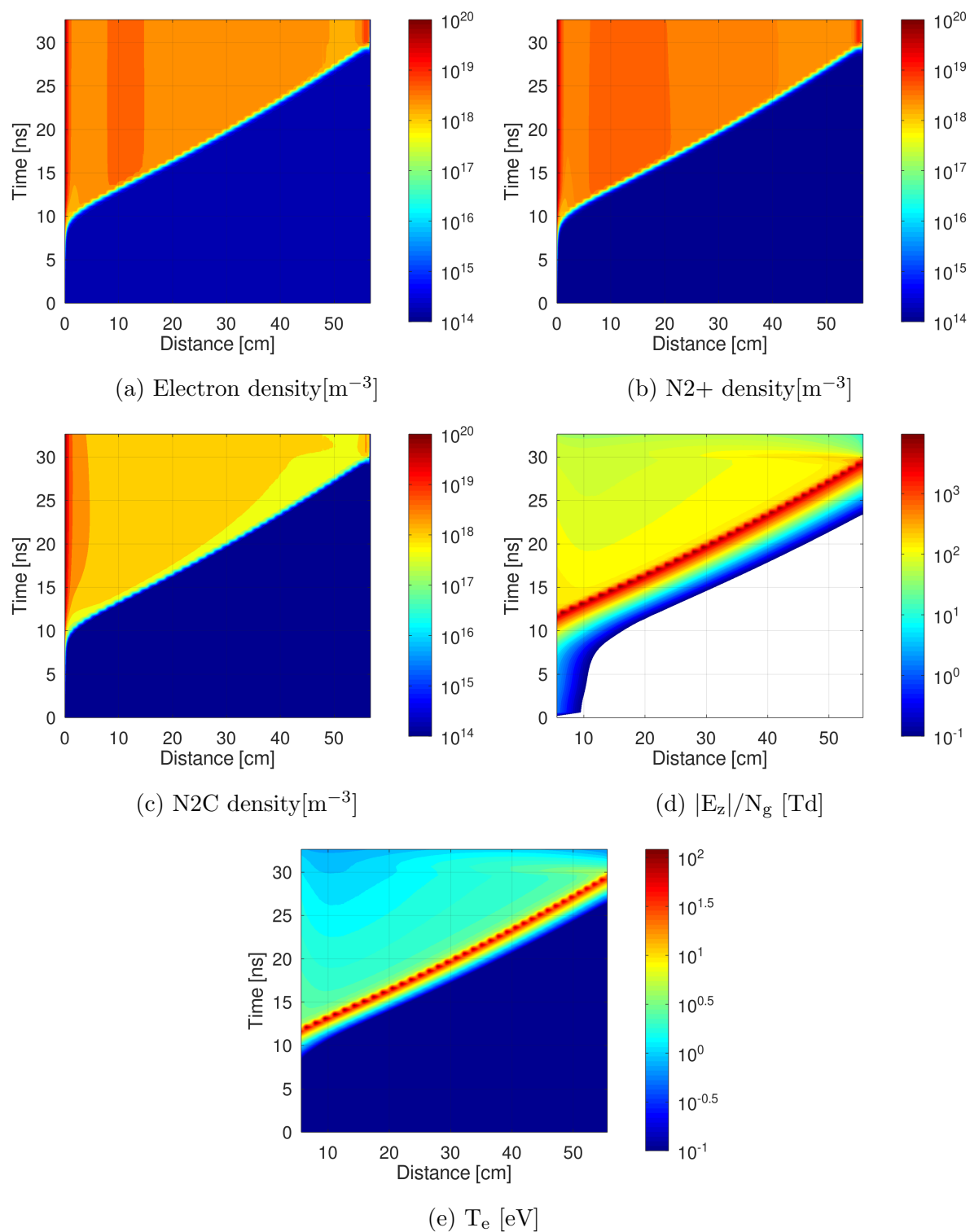


Figure 12: Positive polarity at 5 Torr: Axial distance vs time contour plot of electron, N_2^+ , $\text{N}_2(\text{C}^3\Pi_u)$ species density [m^{-3}], axial component of reduced electric field magnitude [Td] and electron temperature [eV] at $r=0$. All plots in log-scale.

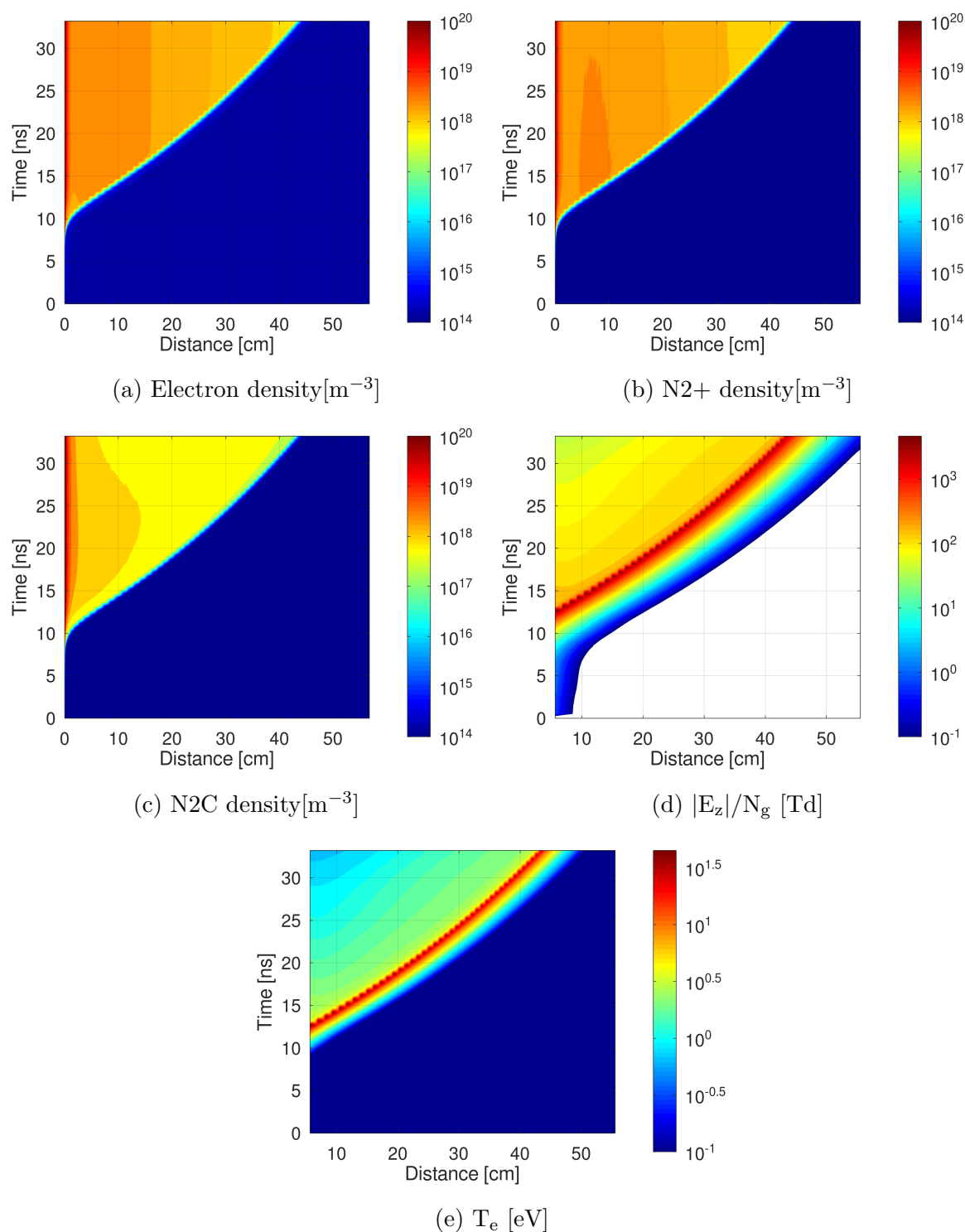


Figure 13: Positive polarity at 10 Torr: Axial distance vs time contour plot of electron, N_2^+ , $\text{N}_2(\text{C}^3\Pi_u)$ species density [m^{-3}], axial component of reduced electric field magnitude [Td] and electron temperature [eV] at $r=0$. Positive polarity at 10 Torr. All plots in log-scale.

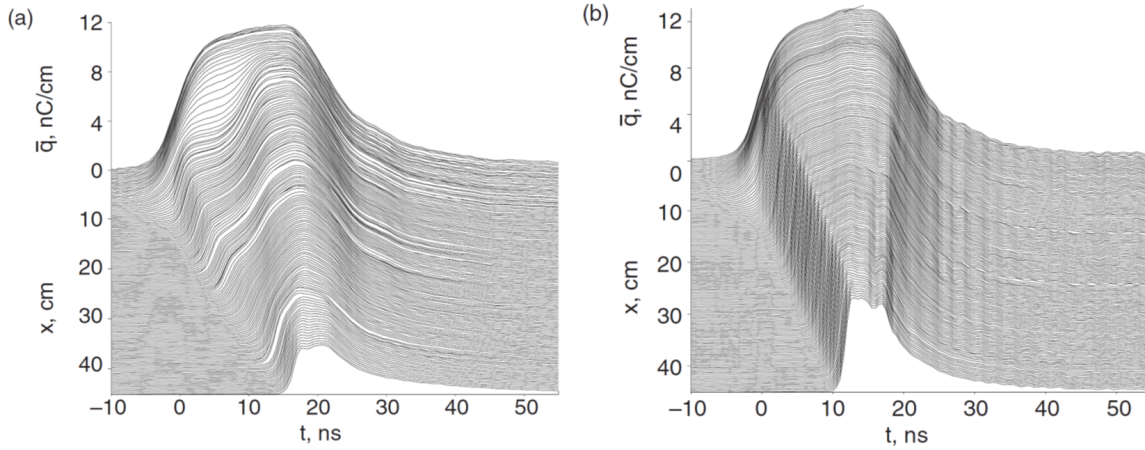


Figure 14: Dynamics of charge measured by capacitive probe [12] for FIW developed in 5 Torr N_2 :(a) negative polarity, (b) positive polarity. The high voltage electrode tip corresponds to coordinate $x = 0$ cm.

indicate the necessity to take into account non-local effects in the front. Non-locality is beyond the scope of this paper, will just mention that the over-population of the EEDF of nanosecond discharge of positive polarity in N_2 at 5 Torr by high energy electrons was indirectly observed in experiments [12].

At $P = 5$ Torr, the calculated FIW propagation speed is substantially higher and equals approximately 3.17 cm/ns. Owing to this high velocity, the FIW is reaching the grounded electrode in less than 30 ns. At $P = 10$ Torr, the FIW speed slightly decreases, reproducing the experimental observations.

The experimental results on charge behaviour in space and time for $P = 5$ Torr nitrogen discharge for both polarities [12] are presented in Fig. 14. Two major differences are observed in the experiment for negative and positive polarities: (i) the presence, at negative polarity, of the developed precursor — a primary wave of low amplitude which the main wave catches up with only at a distance of ~ 30 cm from the high-voltage electrode; (ii) slowing down of the velocity of this precursor with increasing the distance from the high voltage electrode, while the velocity of the ionization wave initiated by a positive polarity pulse on the high-voltage electrode, is constant. The latter effect is well reproduced by numerical simulations of the present work (compare to Figs 9 and 12 respectively).

5.2.3. Temporal profiles of E/N and electron density It is interesting to compare calculated absolute values of the reduced electric field and the electron density as a function of time with the experimental data available in the literature. As far as capacitive probe allows measuring only longitudinal component of the electric field, E_Z , all the discussion below is about the longitudinal component. It is also important to mention that the capacitive probe has a space sensitivity function, and experimentally observed peak of the field should be smoother than in reality.

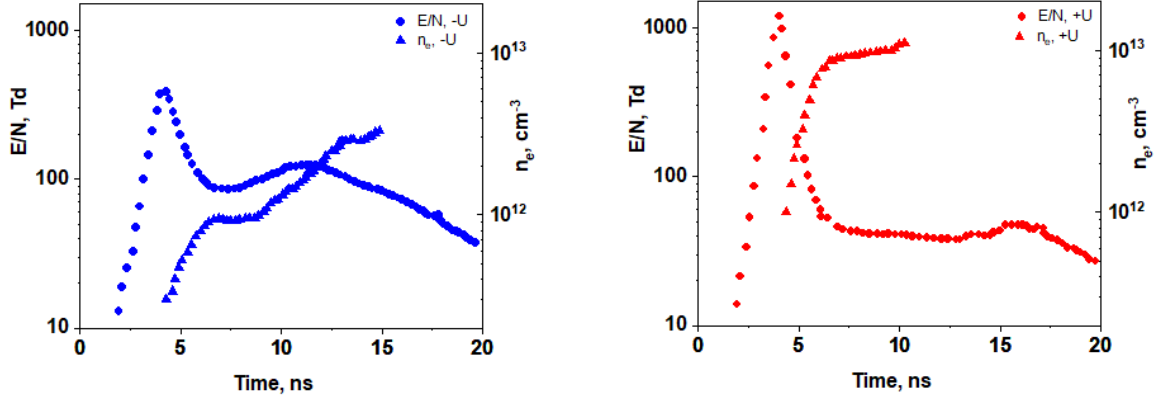
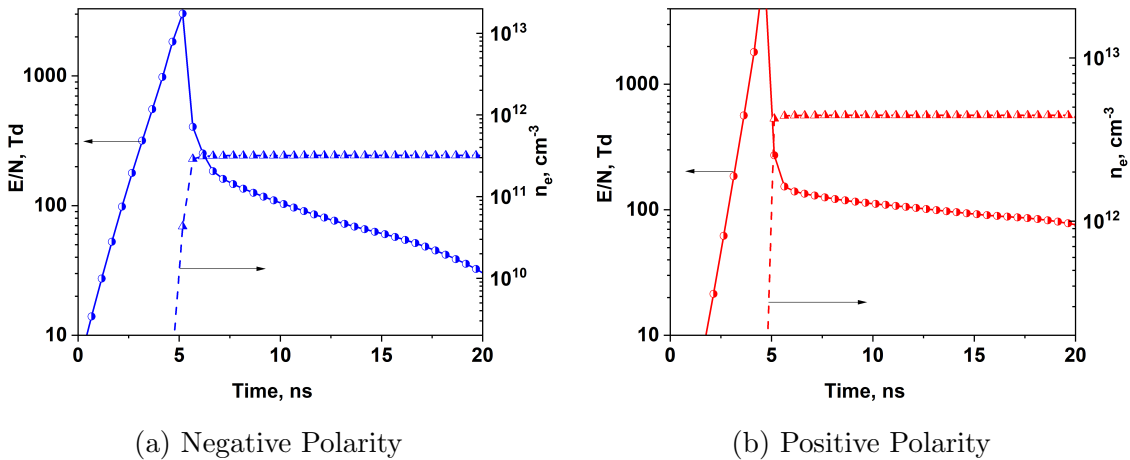


Figure 15: Experimentally measured longitudinal component of the reduced electric field and averaged over the cross-section of the tube electron density at the distance 13 cm from the high-voltage electrode [12]: (a) negative polarity; (b) positive polarity. Nitrogen, pressure 5 torr.

The experimentally measured waveforms of the longitudinal electric field at 13 cm from the high-voltage electrode and of the averaged over the cross-section electron density [12] are presented in Fig. 15. The duration of the high fields in the front of the fast ionization wave is 2-3 ns for any of the polarities. For negative polarity, the peak values of the reduced electric field do not exceed 500 Td, decreasing after the front to approximately 100 Td. For positive polarity, the fields are higher than 1000 Td in the front, decreasing to 40 Td after the front. The electron density is lower at negative polarity, $n_e^{exp} \sim 4 \cdot 10^{12} \text{ cm}^{-3}$, while for positive polarity $n_e^{exp} \sim 10^{13} \text{ cm}^{-3}$.



(a) Negative Polarity

(b) Positive Polarity

Figure 16: Calculated longitudinal reduced electric field and electron density at the distance 13 cm from the high-voltage electrode. Nitrogen, pressure 5 Torr.

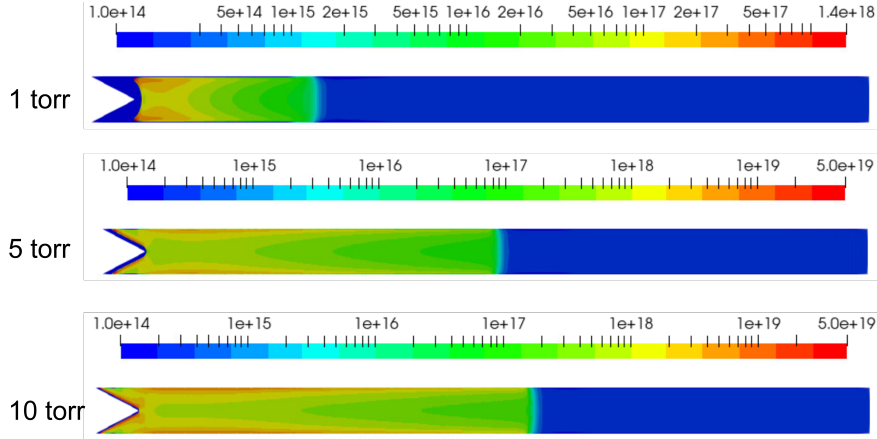


Figure 17: Electron density contours [m^{-3}] for different gas pressure at $t=32.65$ ns. Negative polarity. Min/max values are limited to $10^{14} m^{-3}$ and $5 \times 10^{19} m^{-3}$ respectively for visualization purposes.

Fig. 16 shows the same temporal profiles extracted from the numerical simulations. The calculated E/N is noticeably higher at the plasma front for positive polarity compared to negative polarity, which agrees with the experimental data. Similarly, good agreement is observed on the electron density values, which are lower for negative polarity. After the front, the reduced field is decreasing to values close to the ones observed in the experiments and around 100 Td for both polarities. The build-up of the electron density in numerical modeling is more sharp than in the experiment, while the delay between the field onset and the increase of the electron density is longer than in the experiment. The higher values of both electron density inside the plasma bulk and electron temperature in the FIW front at positive polarity, lead also to higher values of the photoionization source term which is concentrated at the FIW front (i.e. an order of magnitude difference between positive and negative polarities at 5 torr and at the same time-instant). These aspects explain the higher velocity observed under positive polarity, as volume ionization (both electron-impact and photo-related) is stronger in this case.

Will now consider more in details the radial distribution of different components behind the fast ionization wave front, and how this distribution influences $N_2(C^3\Pi_u)$ density, and so the optical emission from the discharge).

5.3. Radial distribution of electron density in the nanosecond discharge. Comparison to the experimental discharge appearance measured by optical imaging.

5.3.1. *Negative polarity* Comparative studies are presented herein for the case of negative polarity. In Fig. 17, we plot the electron density contours in the whole discharge tube, at $t=32.68$ ns for different gas pressure.

It is clearly seen that the discharge propagates further with increasing pressure, featuring a less wide sheath near the HV electrode. The radial distribution of the

electron density is non-uniform in all pressures, with higher densities observed near the dielectric walls. To shed more light on this, in Fig. 18, we plot the radial profiles of electron, N_2^+ and $N_2(C^3\Pi_u)$ densities at $t=32.68$ ns and at a distance of 6.75 cm from the HV electrode's tip for different gas pressures.

All species follow the same radial distribution, showing maximum near the dielectric walls. The density gradient is higher at high pressure than at lower ones e.g. at 10 Torr, the plasma density near the dielectric reaches values of almost $10^{19} m^{-3}$ while at the axis, is one order of magnitude lower. At low pressure (1 Torr) the sheath formed near the dielectric is more pronounced as expected by plasma theory. As the emission relates mainly to the density of $N_2(C^3\Pi_u)$, the numerical results confirm the experimental observations of higher emission near the walls for negative polarity.

5.3.2. Positive polarity Comparative studies are presented herein for the case of positive polarity. In Fig. 19, we plot the electron density contours in the whole discharge tube, at $t=32.68$ ns for different gas pressure.

Here, the discharge propagates further with increasing pressure until it reaches a maximum speed, which is then reduced - at 5 Torr the discharge has already filled in the gap at this time-instant, while at 1 and 10 Torr it stops propagating before bridging the gap. The radial distribution of the electron density is rather uniform at 1 Torr while it begins to take a non-uniform profile with increasing pressure. Near the HV

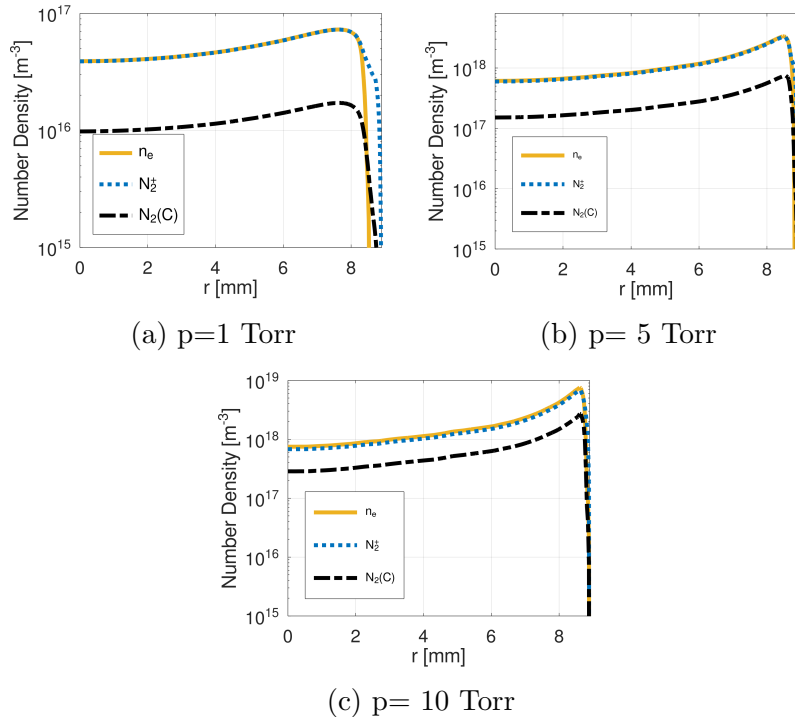


Figure 18: Negative polarity: radial profiles of electron, N_2^+ and $N_2(C^3\Pi_u)$ densities at $t=32.68$ ns and at a distance of 6.75 cm from the HV electrode for different gas pressure.

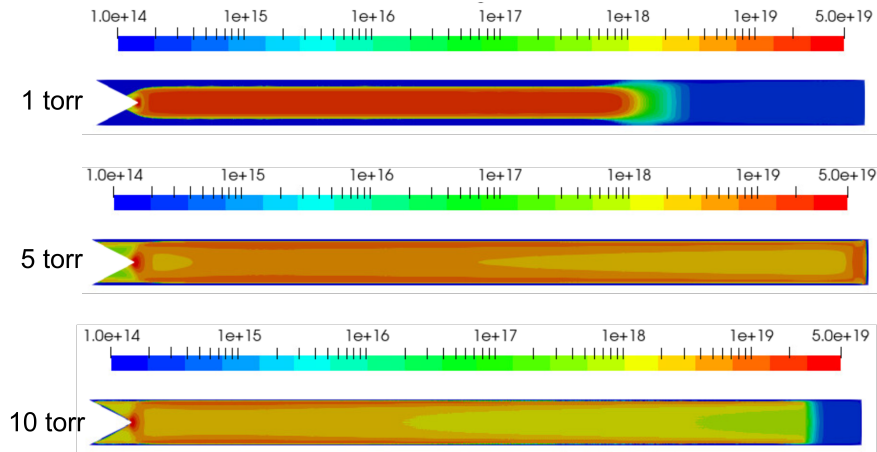


Figure 19: Electron density contours $[m^{-3}]$ for different gas pressure at $t=32.65$ ns. Positive polarity. Min/max values are limited to $10^{14} m^{-3}$ and $5 \times 10^{19} m^{-3}$ respectively for visualization purposes.

electrode, an intense discharge is produced which is in agreement with the experimental emission profiles. As in the negative polarity case above, and to shed more light on this, in Fig. 20, we plot the radial profiles of electron, N_2^+ and $N_2(C^3\Pi_u)$ densities at $t=32.68$ ns and at a distance of 6.75 cm from the HV electrode's tip for different gas pressures.

Similar to the negative polarity case, all species follow the same radial distribution.

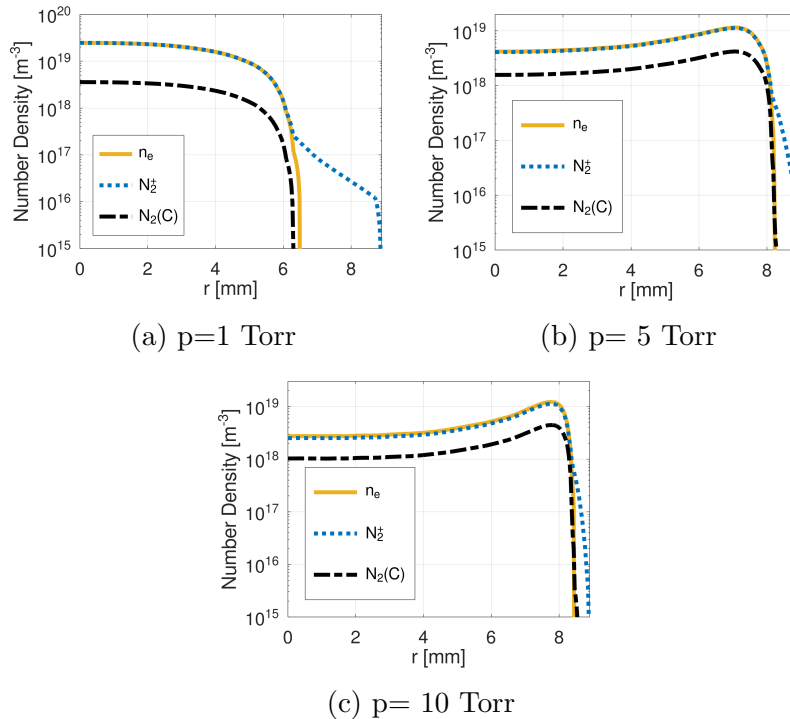


Figure 20: Positive polarity: radial profiles of electron, N_2^+ and $N_2(C^3\Pi_u)$ densities at $t=32.68$ ns and at a distance of 6.75 cm from the HV electrode for different gas pressure.

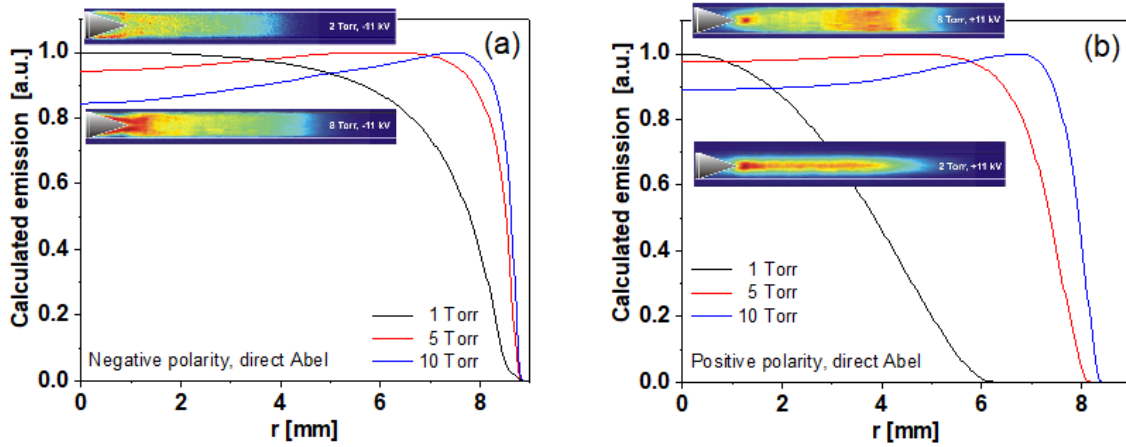


Figure 21: Direct Abel inversion of calculated $N_2(C)$ density profiles in pure N_2 for (a) the negative polarity discharge, the calculated profiles are taken from Fig. 18; (b) the positive polarity discharge, the calculated profiles are taken from Fig. 20. ICCD images for corresponding polarity and pressure experiments in air taken from Fig. 2 are presented in the same figure (see text for details).

In contrast to the negative polarity though, the discharge is more uniform at low pressure, showing maximum near the axis or presenting a smoother density gradient. As the pressure increases, the discharge seems to obtain a non-uniform radial profile and approach the distribution of the negative polarity case. The sheaths formed near the dielectric are thicker at all pressure levels in this case.

The change of radial profiles observed between the negative and positive polarities is related to the presence of the dielectric and associated surface charging effects. Similar to nanosecond surface Dielectric Barrier Discharges (DBDs) [65], the effects of surface charge accumulation as well as secondary electron emission on the dielectric surfaces, which are both dependent on the voltage polarity and thus the orientation of the electric field vectors which dictate charged species transport towards the dielectric tube, seem to play an important role on the discharge dynamics.

The calculated distribution of discharge emission over the cross-section reproduces the main features observed in the experiment. To provide better comparison, Fig. 21 presents a direct Abel transform of the calculated radial distribution of $N_2(C^3\Pi_u)$ density taken from Figs 18 and 20. The forward Abel transform is done using the online PlasmAbel software [66]. The ICCD images of $N_2(C^3\Pi_u) \rightarrow N_2(B^3\Pi_g)$ emission in air are shown in the same figure (see Sec. 2 for more details). Excellent qualitative correlation between ICCD imaging and $[N_2(C^3\Pi_u)]$ calculations is observed. Will underline that, in spite of visible “homogeneity” with a weakly expressed minimum, at negative polarity on the high-voltage electrode, the discharge develops near walls, leaving the near-axis part “empty”. The difference between the density of particles produced near the walls and on the axis can reach an order of magnitude or more (see Fig. 18), and this should be taken

into account in any measurements of the density of active species. At positive polarity of the high-voltage electrode, especially at low pressures, the discharge develops along the axis, the distance between a quasi-neutral plasma and the walls (sheath thickness) can reach 2 mm for a tube diameter of 20 mm.

6. Conclusions

In this study, fast ionization waves (FIWs) propagating along a cylindrical coaxial discharge setup are investigated using 2D-axisymmetric numerical modeling. FIWs are initiated by a single nanosecond pulse with a 27 kV amplitude applied to the high-voltage electrode. The pulse has a FWHM of 25 ns and a rise time of 4 ns, corresponding to a voltage increase rate of $\partial U/\partial t \approx 6$ kV/ns. Both negative and positive polarity pulses are considered. The study examines pressures ranging from 1 to 10 Torr in molecular nitrogen. The numerical results are validated against available experimental data.

Consistent with experimental observations, the numerical modeling reveals a characteristic temporal behavior of the FIW front: the electron density builds up following a sharp and brief (a few nanoseconds) peak in the electric field. The peak electric field reaches approximately 10^3 Td, with values 20–30% higher for positive polarity pulses. After the front, the field drops to around ~ 100 Td. The electron density behind the FIW front is in the range of $10^{11} - 10^{12}$ cm³/s for FIWs initiated by negative polarity pulses and $10^{12} - 10^{13}$ cm³/s for FIWs initiated by positive polarity pulses. The synchronized waveforms of $E/N(t)$ and $n_e(t)$ observed in experiments are reproduced by the numerical modeling.

For both polarities, FIWs originate at the high-voltage electrode and propagate along the tube. The numerically obtained FIW velocities are in good agreement with experimental results, exhibiting a clear maximum as a function of pressure. For a given voltage amplitude and discharge tube diameter, this maximum occurs at 5–6 Torr, with FIW velocities of 2–3 cm/ns for negative polarity pulses and 3–4 cm/ns for positive polarity pulses.

Furthermore, the radial distributions of densities of electrons, ions and N₂(C³Π_u) molecules are analyzed. The numerical modeling indicates similar radial distributions for $n_e(t)$ and [N₂(C³Π_u)] for all considered cases, while a well-pronounced sheath with a non-compensated charge of positive ions is observed near the tube wall. The sheath thickness reaches about 2 mm at $P = 1$ Torr for a positive polarity pulse. The density of N₂(C³Π_u) reaches $10^{11} - 10^{11}$ cm⁻³, with higher values for positive polarity pulses. The pressure-dependent radial distribution of optical emission is well explained by the modeling and shows a good agreement with experimental observations. At negative polarity, the FIW in nitrogen develops near the tube walls, resulting in electron and N₂(C³Π_u) densities in the tube center that can be an order of magnitude lower. At positive polarity and low pressures, the significant sheath thickness creates the impression that the FIW propagates in a beam-like mode along the tube axis.

Thus, the proposed modeling approach successfully reproduces the key features of

FIW development in nitrogen at moderate pressures and can be used as a valuable tool for optimizing nanosecond discharge experiments. Further parametrization for a broader pressure range, different gas mixtures (e.g. air), tube geometries (e.g. diameter to length ratio) and pulse characteristics as well as investigation of the sensitivity of the results to chosen parameters (namely the chosen plasma-chemistry set) are left for future studies.

Acknowledgments

This work was supported by the European Union Project CAIPIRINH3A, under the GA number 101191768. Views and opinions expressed are however those of the author(s) only and do not necessarily reflect those of the European Union or CINEA. Neither the European Union nor the granting authority can be held responsible for them. The work of S.M.Starikovskaia was also partially supported by the Energy4Climate Interdisciplinary Center (E4C) of IP Paris and Ecole des Ponts ParisTech in the framework of the 3rd Programme d'Investissements d'Avenir [ANR-18-EUR-0006-02] and by Cellule Énergie du CNRS (PEPS 2024 Project ZEPHiR).

References

- [1] B M Goldberg, T Hoder, and R Brandenburg. Electric field determination in transient plasmas: *in-situ* & non-invasive methods. *Plasma Sources Sciences and Technology*, 31:073001, 2022.
- [2] Matthew Hay, Pradeep Parajuli, and Waruna D Kulatilaka. Simultaneous detection of three chemical species (no, o, o₂) using a single broadband femtosecond laser. *Proceedings of the Combustion Institute*, 39 (1):1435–1444, 2023.
- [3] Andrey Starikovskiy and Nickolay Aleksandrov. Plasma-assisted ignition and combustion. *Progress in Energy and Combustion Science*, 39(1):61–110, 2013.
- [4] SM Starikovskaia. Plasma-assisted ignition and combustion: nanosecond discharges and development of kinetic mechanisms. *Journal of Physics D: Applied Physics*, 47(35):353001, 2014.
- [5] Yiguang Ju and Wenting Sun. Plasma assisted combustion: Dynamics and chemistry. *Progress in Energy and Combustion Science*, 48:21–83, 2015.
- [6] Sergey B Leonov, Igor V Adamovich, and Victor R Soloviev. Dynamics of near-surface electric discharges and mechanisms of their interaction with the airflow. *Plasma Sources Science and Technology*, 25(6):063001, 2016.
- [7] M Samimy, N Webb, and A Esfahani. Reinventing the wheel: Excitation of flow instabilities for active flow control using plasma actuators. *Journal of Physics D: Applied Physics*, 52(52):354002, 2019.
- [8] R Limanowski, D Yan, L Li, and M Keidar. Preclinical cold atmospheric plasma cancer treatment (review). *Cancers*, 14:3461, 2022.
- [9] JJ Thomson. *Researches in Electricity and Magnetism*. Oxford: Clarendon, 1893.
- [10] LM Vasilyak, SV Kostyuchenko, NN Kudryavtsev, and IV Filyugin. High-speed ionization waves at an electric breakdown. *Phys.–Uspekhi*, 163:263–286, 1994.
- [11] N B Anikin, S V Pancheshnyi, S M Starikovskaia, and A Yu Starikovskii. Breakdown development at high overvoltage: electric field, electronic level excitation and electron density. *Journal of Physics D: Applied Physics*, 31(7):826, 1998.
- [12] NB Anikin, SM Starikovskaia, and A Yu Starikovskii. Polarity effect of applied pulse voltage on

- the development of uniform nanosecond gas breakdown. *Journal of Physics D: Applied Physics*, 35(21):2785, 2002.
- [13] NB Anikin, SM Starikovskaia, and A Yu Starikovskii. Study of the oxidation of alkanes in their mixtures with oxygen and air under the action of a pulsed volume nanosecond discharge. *Plasma physics reports*, 30(12):1028–1042, 2004.
- [14] NB Anikin, NA Zavialova, SM Starikovskaia, and AYu Starikovskii. Nanosecond discharge development in long tubes. *IEEE Transactions on Plasma Science*, 36(4):902–903, 2008.
- [15] SM Starikovskaia, A Yu Starikovskii, and DV Zatsepin. The development of a spatially uniform fast ionization wave in a large discharge volume. *Journal of Physics D: Applied Physics*, 31(9):1118, 1998.
- [16] S V Pancheshnyi, S M Starikovskaia, and A Yu Starikovskii. Population of nitrogen molecule electron states and structure of the fast ionization wave. *Journal of Physics D: Applied Physics*, 32(17):2219, 1999.
- [17] S V Pancheshnyi, S M Starikovskaia, and A Yu Starikovskii. Collisional desactivation of $N_2(C^3\Pi_u, v = 0, 1, 2, 3)$ states by N_2 , O_2 , H_2 and H_2O molecules. *Chemical Physics*, 262:349–357, 2000.
- [18] SM Starikovskaia, NB Anikin, SV Pancheshnyi, DV Zatsepin, and A Yu Starikovskii. Pulsed breakdown at high overvoltage: development, propagation and energy branching. *Plasma Sources Science and Technology*, 10(2):344, 2001.
- [19] SM Starikovskaia, NB Anikin, SV Pancheshnyi, and A Yu Starikovskii. Time-resolved emission spectroscopy and its applications to the study of pulsed nanosecond high-voltage discharges. *Selected Research Papers on Spectroscopy of Nonequilibrium Plasma at Elevated Pressures, Vladimir N. Ochkin, Editor, Proceedings of Society of Photo-Optical Instrumentation Engineers (SPIE)*, 4460:63–73, 2002.
- [20] George V Naidis, Victor F Tarasenko, Natalia Yu Babaeva, and Mikhail I Lomaev. Subnanosecond breakdown in high-pressure gases. *Plasma Sources Science and Technology*, 27(1):013001, 2018.
- [21] Ute Ebert, Wim van Saarloos, and Christiane Caroli. Streamer propagation as a pattern formation problem: planar fronts. *Physical review letters*, 77(20):4178, 1996.
- [22] OA Sinkevich and DN Gerasimov. Propagation of super-high-speed ionizing waves in long shielded tubes. *Journal of Physics D: Applied Physics*, 33(1):54, 2000.
- [23] John P Verboncoeur. Particle simulation of plasmas: review and advances. *Plasma Physics and Controlled Fusion*, 47(5A):A231, 2005.
- [24] Charles K Birdsall and A Bruce Langdon. *Plasma physics via computer simulation*. CRC press, 2018.
- [25] DF Rodríguez-Patiño, S Ramírez, JS Salcedo-Gallo, JH Hoyos, and E Restrepo-Parra. Implementation of the two-dimensional electrostatic particle-in-cell method. *American Journal of Physics*, 88(2):159–167, 2020.
- [26] WJM Brok, J Van Dijk, MD Bowden, JJAM Van der Mullen, and GMW Kroesen. A model study of propagation of the first ionization wave during breakdown in a straight tube containing argon. *Journal of Physics D: Applied Physics*, 36(16):1967, 2003.
- [27] Pedro Viegas, Elmar Slikboer, Zdenek Bonaventura, Enric Garcia-Cauarel, Olivier Guaitella, Ana Sobota, and Anne Bourdon. Quantification of surface charging memory effect in ionization wave dynamics. *Scientific Reports*, 12(1):1181, 2022.
- [28] Keisuke Takashima, Igor V Adamovich, Uwe Czarnetzki, and Dirk Luggenhölscher. Development of fast ionization wave discharges at high pulse repetition rates. *Plasma Chemistry and Plasma Processing*, 32:471–493, 2012.
- [29] Keisuke Takashima, Igor V Adamovich, Zhongmin Xiong, Mark J Kushner, Svetlana Starikovskaia, Uwe Czarnetzki, and Dirk Luggenhölscher. Experimental and modeling analysis of fast ionization wave discharge propagation in a rectangular geometry. *Physics of Plasmas*, 18(8), 2011.
- [30] Bang-Dou Huang, Emile Carbone, Keisuke Takashima, Xi-Ming Zhu, Uwe Czarnetzki, and Yi-Kang Pu. The effect of the pulse repetition rate on the fast ionization wave discharge. *Journal*

- of *Physics D: Applied Physics*, 51(22):225202, 2018.
- [31] Andrei V Klochko, Svetlana M Starikovskaia, Zhongmin Xiong, and Mark J Kushner. Investigation of capillary nanosecond discharges in air at moderate pressure: comparison of experiments and 2d numerical modelling. *Journal of Physics D: Applied Physics*, 47(36):365202, 2014.
- [32] Yifei Zhu, Svetlana M Starikovskaia, Natalia Yu Babaeva, and Mark J Kushner. Scaling of pulsed nanosecond capillary plasmas at different specific energy deposition. *Plasma Sources Science and Technology*, 29(12):125006, 2020.
- [33] Xiancong Chen, Yifei Zhu, Yun Wu, Jinbo Hao, Xiaoguang Ma, and Pengfei Lu. Modeling of fast ionization waves in pure nitrogen at moderate pressure. *Plasma Sources Science and Technology*, 30(6):065002, 2021.
- [34] M Timshina, S Eliseev, N Kalinin, D Belsky, A Samokhvalov, K Sergushichev, A Smirnov, and V Burtsev. Numerical investigation of capillary discharge initiation by fast ionization waves. *Journal of Electrostatics*, 107:103485, 2020.
- [35] Timothy Wong, Igor Timoshkin, Scott MacGregor, Mark Wilson, and Martin Given. A computational study on the effects of fast-rising voltage on ionization fronts initiated in sub-mm air and co 2 gaps. *Scientific Reports*, 14(1):1185, 2024.
- [36] Dmitry Levko and Laxminarayan L Raja. Influence of field emission on the propagation of cylindrical fast ionization wave in atmospheric-pressure nitrogen. *Journal of Applied Physics*, 119(15), 2016.
- [37] Dmitry Levko and Laxminarayan L Raja. Kinetics of the fast ionization waves with runaway electrons. *Physics of Plasmas*, 30(7), 2023.
- [38] N D Lepikhin, N A Popov, and S M Starikovskaia. Fast gas heating and radial distribution of active species in nanosecond capillary discharge in pure nitrogen and n2:o2 mixtures. *Plasma Sources Science and Technology*, 27(5):055005, 2018.
- [39] C A Pavan, S R Rao, and C Guerra-Garcia. Tutorial: Electrical measurements in nanosecond pulsed plasma reactors. *Journal of Physics D: Applied Physics*, 2024. Accepted Manuscript online 27 August 2024.
- [40] ND Lepikhin, NA Popov, and SM Starikovskaia. Fast gas heating and radial distribution of active species in nanosecond capillary discharge in pure nitrogen and n2: O2 mixtures. *Plasma Sources Science and Technology*, 27(5):055005, 2018.
- [41] Konstantinos Kourtzanidis, Guillaume Dufour, and François Rogier. Self-consistent modeling of a surface ac dielectric barrier discharge actuator: in-depth analysis of positive and negative phases. *Journal of Physics D: Applied Physics*, 54(4):045203, 2020.
- [42] G Dufour and F Rogier. Numerical modeling of dielectric barrier discharge based plasma actuators for flow control: the copaier/cedre example. *Aerospace Lab*, (10), 2015.
- [43] Anne Bourdon, VP Pasko, Ningyu Y Liu, Sébastien Célestin, Pierre Ségur, and Emmanuel Marode. Efficient models for photoionization produced by non-thermal gas discharges in air based on radiative transfer and the helmholtz equations. *Plasma Sources Science and Technology*, 16(3):656, 2007.
- [44] Tugba Piskin, Vladlen A Podolsky, Sergey O Macheret, and Jonathan Poggie. Challenges in numerical simulation of nanosecond-pulse discharges. *Journal of Physics D: Applied Physics*, 52(30):304002, 2019.
- [45] GK Grubert, MM Becker, and D Loffhagen. Why the local-mean-energy approximation should be used in hydrodynamic plasma descriptions instead of the local-field approximation. *Physical Review E*, 80(3):036405, 2009.
- [46] ZHU Yifei. Photo-ionization parameter calculator release 1.0. 2020.
- [47] Yifei Zhu, Yun Wu, and Jianzhong Li. Photopic: calculate photo-ionization functions and model coefficients for gas discharge simulations. *arXiv preprint arXiv:2005.10021*, 2020.
- [48] GW Penney and GT Hummert. Photoionization measurements in air, oxygen, and nitrogen. *Journal of applied physics*, 41(2):572–577, 1970.
- [49] K Kourtzanidis. Full cycle, self-consistent, two-dimensional analysis of a packed bed dbd reactor for

- plasma-assisted splitting: spatiotemporal inhomogeneous, glow to streamer to surface discharge transitions. *Plasma Sources Science and Technology*, 32(10):105016, 2023.
- [50] Donald L Scharfetter and Hermann K Gummel. Large-signal analysis of a silicon read diode oscillator. *IEEE Transactions on electron devices*, 16(1):64–77, 1969.
- [51] Nguyen Tuan Dung, Christophe Besse, and François Rogier. An implicit time integration approach for simulation of corona discharges. *Computer Physics Communications*, 294:108906, 2024.
- [52] GJM Hagelaar and GMW Kroesen. Speeding up fluid models for gas discharges by implicit treatment of the electron energy source term. *Journal of Computational Physics*, 159(1):1–12, 2000.
- [53] Andrea Villa, Luca Barbieri, Marco Gondola, and Roberto Malgesini. An asymptotic preserving scheme for the streamer simulation. *Journal of Computational Physics*, 242:86–102, 2013.
- [54] GJM Hagelaar and LC Pitchford. Solving the boltzmann equation to obtain electron transport coefficients and rate coefficients for fluid models. *Plasma Sources Science and Technology*, 14(4):722, 2005.
- [55] Phelps database, www.lxcat.net, retrieved on november 28, 2023.
- [56] T. Murphy and NM (USA) Los Alamos National Lab. Total and differential electron collision cross sections for O2 and N2, January 2025.
- [57] Deniz Cinar. *Relativistic electrons in electric discharges*. Phd thesis, DTU Space, 2014. Available at <https://orbit.dtu.dk/en/publications/relativistic-electrons-in-electric-discharges>.
- [58] Larry A Viehland and Charles C Kirkpatrick. Relating ion/neutral reaction rate coefficients and cross-sections by accessing a database for ion transport properties. *International journal of mass spectrometry and ion processes*, 149:555–571, 1995.
- [59] IA Kossyi, A Yu Kostinsky, AA Matveyev, and VP Silakov. Kinetic scheme of the non-equilibrium discharge in nitrogen-oxygen mixtures. *Plasma Sources Science and Technology*, 1(3):207, 1992.
- [60] Mario Capitelli, Carlos M Ferreira, Boris F Gordiets, and Alexey I Osipov. *Plasma kinetics in atmospheric gases*, volume 31. Springer Science & Business Media, 2013.
- [61] Christophe Geuzaine and Jean-François Remacle. A three-dimensional finite element mesh generator with built-in pre-and post-processing facilities. *Int. J. Numer. Methods Eng*, 11:79, 2020.
- [62] N. B. Anikin. *Experimental study of electrodynamic characteristics of the fast ionization waves in molecular gases*. PhD thesis, PhD Thesis, Moscow Institute of Physics and Technology, 2000. (in Russian).
- [63] N L Aleksandrov, S V Kindysheva, A A Kirpichnikov, I N Kosarev, S M Starikovskaia, and A Yu Starikovskii. Plasma decay in n₂, co₂ and h₂o excited by high-voltage nanosecond discharge. *Journal of Physics D: Applied Physics*, 40(15):4493, 2007.
- [64] S M Starikovskaia. Energy distribution over the internal degrees of freedom in gas for a high-voltage nanosecond discharge in the case of o₂ dissociation. *Plasma Physics Reports (ISSN 1063-780X) Transl. of Fizika Plazmy*, 21(6):541–547, 1995.
- [65] V R Soloviev, A M Konchakov, V M Krivtsov, and N L Aleksandrov. Numerical simulation of a surface barrier discharge in air. *Plasma Physics Reports*, 34(7):594–608, 2008.
- [66] Plasmabel: easy abel transformator for plasma optical measurements, <http://www.plasma-tech.net/plasmabel/>.